Journal of Water Process Engineering 91 (2026) 110500

Contents lists available at ScienceDirect

Journal of Water Process Engineering

journal homepage: www.elsevier.com/locate/jwpe

Charge-dependent removal in water treatment using NaOH-modified olive stone: Batch and fixed-bed evaluation of Pb(II), Cd(II), and As(V)

Jose A. Valeriano-Zapana [a,*], Vera D. Condori-Yupanqui [a], Paulino F. Rios-Zapana [a], Juana J. Melendez-Mier [a], Leonel A. Paccosonco-Sucapuca [a], Corina A. Vera-Gonzáles [b], Juan A. Lopa-Bolívar [c]

[a] Laboratorio de Procesos Industriales y Ambientales, Escuela Profesional de Ingeniería Ambiental, Universidad Nacional de Moquegua - UNAM, Ilo, Peru
[b] Laboratorio de Preparación, Caracterización e Identificación de Nanomateriales (LAPCINANO), Centro de Investigacion Aplicada y Laboratorios Especializados (CIALE), Universidad Nacional de San Agustín de Arequipa, Arequipa, Peru
[c] Departamento Académico de Química, Universidad Nacional de San Agustín de Arequipa, Arequipa, Peru

ARTICLE INFO

Editor: Soraya Malinga

Keywords:
Olive stone
Water treatment
Fixed-bed column
Charge-dependent removal
Arsenate

ABSTRACT

Low-cost biosorbents from agricultural residues are promising for water treatment but are usually evaluated for single contaminants under batch conditions only. We assessed the charge-dependent removal of cationic Pb(II) and Cd(II) and anionic As(V) by NaOH-modified olive stone (*Olea europaea* L.) in batch and fixed-bed systems, using a common biosorbent preparation and parallel protocols. NaOH treatment shifted the pH_{PZC} from 4.47 to 6.83 and produced FTIR changes consistent with ester-bond saponification and greater exposure of carboxylate and hydroxyl groups. Under optimized batch conditions, Pb(II) removal reached 99.57% and remained above 98.9% across independent series, although removal at pH 6.8–8.0 should be interpreted as an upper bound because phosphate buffering may contribute to lead phosphate precipitation. Cd(II) removal varied from 5.5% to 99.7% depending on operational conditions, with the upper value (99.72%) obtained at 15 g L^{-1} in the dose × size factorial; the variability is largely attributable to operational differences between experimental series (dose, contact time, replication regime); a single biosorbent preparation was used throughout, so batch-to-batch variability could not be evaluated. As(V) removal remained below 8% under all conditions. Fixed-bed breakthrough curves were adequately described by Thomas and Yoon–Nelson models ($R^2 > 0.97$), with column capacities of 4.01 mg g^{-1} for Cd(II) (extrapolated) and 2.27 for Pb(II); the 1.77 value for As(V) reflects transient column retention rather than true uptake. NaOH-modified olive stone is robust for Pb(II), conditional for Cd(II), and unsuitable for As(V), supporting contaminant-specific biosorbent selection.

1. Introduction

Heavy metal and metalloid contamination in aquatic systems remains a major global environmental and public-health concern, and its management in industrial, mining, and agricultural effluents represents a persistent challenge for water-treatment practice. Lead and cadmium are non-biodegradable, bioaccumulative, and toxic even at low concentrations, whereas arsenic contamination continues to affect large populations worldwide through drinking water exposure [1–4]. A key difficulty for remediation is that these contaminants differ fundamentally in aqueous speciation: Pb and Cd occur as cationic species, whereas arsenic in oxic waters is commonly present as anionic arsenate oxyanions [5]. As a result, treatment materials that perform well for cationic metals often show limited affinity for anionic contaminants [6,7].

Conventional metal-removal technologies such as chemical precipitation, ion exchange, membrane filtration, and electrochemical treatment are effective but constrained by high operating costs, sludge generation, and reduced efficiency at low solute concentrations [8,9]. Biosorption has received sustained attention as a low-cost alternative because of its operational simplicity and potential for metal recovery [10–12]. Agricultural residues are especially attractive because they are abundant, inexpensive, and rich in functional groups capable of interacting with dissolved metals [13,14], but lignocellulosic biosorbents generally favor cation uptake over anion uptake, a limitation that becomes especially relevant in mixed-contaminant waters [7,15].

Chemical modification is commonly used to improve biosorbent

* Corresponding author.
E-mail address: jvalerianoz@unam.edu.pe (J.A. Valeriano-Zapana).

https://doi.org/10.1016/j.jwpe.2026.110500
Received 25 April 2026; Received in revised form 6 June 2026; Accepted 28 June 2026
Available online 30 June 2026
2214-7144/© 2026 Elsevier Ltd. All rights are reserved, including those for text and data mining, AI training, and similar technologies.

performance. NaOH treatment has been widely applied to lignocellulosic materials because it promotes partial delignification, alters porosity, and increases the exposure of oxygen-containing surface groups through alkaline hydrolysis and deacetylation [16,17]. These changes often enhance the uptake of cationic metals such as Pb(II) and Cd(II) [18,19], but may simultaneously reduce affinity for anionic species such as arsenate. Despite this plausible charge-dependent behavior, few studies have evaluated cationic and anionic contaminants in parallel using the same NaOH-modified biosorbent under comparable experimental conditions.

Olive stone, the main solid by-product of olive processing, is a promising biosorbent candidate generated in large quantities globally and in the olive-producing areas of southern Peru [20–23]. Its lignocellulosic matrix provides oxygen-containing functional groups that can interact with dissolved metals [24,25]. Previous studies have demonstrated the utility of olive-derived materials for removing individual cationic metals, particularly Pb(II) and Cd(II) [26,27]. However, to our knowledge, no study has systematically compared the behavior of cationic Pb(II) and Cd(II) against anionic As(V) using the same olive stone-based biosorbent under parallel conditions. The local availability of this residue in olive-producing regions offers a logistical advantage for deploying biosorbent-based treatment systems where contamination from mining and agricultural activities is a recurrent concern.

We hypothesized that NaOH modification of olive stone would enhance the uptake of cationic species [Pb(II), Cd(II)] while limiting retention of anionic As(V), and that this charge-dependent performance would manifest consistently across both batch and fixed-bed column operation. To test this hypothesis, we (i) characterized the biosorbent before and after alkaline treatment (SEM, BET, FTIR, pH_{PZC}) to establish the surface-chemistry basis for charge-dependent behavior; (ii) evaluated batch removal of Pb(II), Cd(II), and As(V) under a factorial design covering pH (4.0–8.5), particle size (75–300 μm), and biosorbent dosage (5–15 g L^{-1}), with ANOVA quantified by partial eta-squared and partial omega-squared effect sizes; (iii) analyzed the kinetics of uptake by nonlinear regression against pseudo-first-order, pseudo-second-order, and intraparticle diffusion models; and (iv) assessed continuous-flow performance in fixed-bed columns, with breakthrough curves fitted to the Thomas and Yoon–Nelson models. The resulting dataset is used to identify the operational boundaries of NaOH-modified olive stone as a biosorbent for cation-dominated, anion-dominated, and mixed cation–anion effluents.

The present study focuses on As(V) as the anionic test species and does not address As(III). As(V) was selected because it is fully ionized across the pH range tested ($H_2AsO_4^-$ at pH 2–7; $HAsO_4^{2-}$ at pH 7–11) and therefore provides a clean test of charge-dependent selectivity against cationic Pb(II) and Cd(II), and because it is the thermodynamically stable arsenic species under the oxic conditions characteristic of the surface and industrial waters that constitute the principal target matrix. As(III), which dominates in reducing groundwaters and is more toxic and mobile, exists predominantly as the neutral $H_3AsO_3^0$ species at circumneutral pH (pKa ≈ 9.2) and would therefore confound the test of charge-dependent behavior. Evaluation under reducing conditions and against As(III), likely requiring an oxidative pre-treatment or an iron-modified material, is identified as a priority next step (Section 4.8).

2. Materials and methods

Throughout this study, the olive stone biosorbent derived from *Olea europaea* L. pomace was designated according to its processing stage: NC for the native untreated biosorbent, CT for the NaOH-treated biosorbent, and DA for the biosorbent collected after Pb(II) adsorption experiments.

2.1. Olive stone preparation and conditioning

A total of 21.5 kg of raw olive pomace was collected from Aceitunas de Ilo S.A. (El Algarrobal, Ilo, Peru). The pomace was washed with deionized water, and the pulp was removed manually, yielding approximately 10 kg of wet olive stone fraction. The isolated olive stones were further washed with boiling deionized water to remove residual soluble organic matter and lipids, then dried at 105 °C for 24 h following Martín-Lara et al. [27] and stored in sealed containers at room temperature prior to size reduction. A full mass balance, including wet-basis yield and dry-basis processing recovery, is provided in Table S1. The dried material was crushed in a hammer mill and sieved through ASTM E11 standard sieves to obtain three nominal particle-size fractions of 75, 150, and 300 μm. The sieved fractions were then oven-dried at 50 °C for 24 h to ensure constant moisture before experimental use [28].

2.2. Alkaline modification of olive stone

The three particle-size fractions were subjected to alkaline modification with 0.1 M NaOH at a liquid-to-solid ratio of 100 mL g^{-1}. Suspensions were agitated at 600 rpm for 24 h at room temperature (20 ± 2 °C). After sedimentation for 2–4 h, the biosorbent was washed with distilled water until the rinse water reached near-neutral pH, oven-dried at 60 °C for 24 h, and stored in airtight bags. The final moisture content was 5–6%. This modified material was designated CT [29]. All experiments reported in this study, including batch factorial assays, kinetic experiments, equilibrium tests, and fixed-bed column runs, used CT material from a single NaOH-modification preparation. Consequently, batch-to-batch variability in the alkaline modification could not be evaluated in this study and is acknowledged as a limitation (Section 4.8).

2.3. Physicochemical characterization

Surface morphology was examined by scanning electron microscopy (SEM; Zeiss Supra 40, Universidad Nacional de Ingeniería, Lima, Peru) operated in variable-pressure mode at an accelerating voltage of 20 kV using an SE1 detector and a working distance of 9.5 mm. Dried biosorbent samples were mounted on aluminum stubs using conductive carbon tape and analyzed without metallic coating. Specific surface area was determined from N_2 adsorption isotherms at 77 K using the Brunauer–Emmett–Teller (BET) equation over the relative-pressure range P/P_0 = 0.05–0.30 on a GEMINI VII 2390 analyzer (Micromeritics). Samples were outgassed under vacuum prior to analysis according to the manufacturer's recommended protocol. DA-derived average pore diameter was estimated from the N_2 adsorption branch and is reported in Table S6. Functional groups were analyzed by Fourier-transform infrared spectroscopy (FTIR; PerkinElmer Frontier) using the KBr pellet method in transmittance mode over the range 4000–450 cm^{-1}. Dried samples were finely ground and mixed with spectroscopic-grade KBr at a sample:KBr ratio of approximately 1:100 (*w*/w). Spectra were collected at 4 cm^{-1} resolution with 32 scans per sample. NC, CT, and DA samples were analyzed by all three techniques.

Chemical characterization was carried out on NC and CT. Ash was determined gravimetrically at 600 °C for 4 h (AOAC 2.173); Ca + Mg by EDTA complexometric titration (AOAC 968.08); Fe by thiocyanate colorimetry at 480 nm (NTE INEN 1908:2013); P by the ascorbic acid–phosphomolybdate method at 885 nm (AOAC 985.11); and cellulose, hemicellulose and lignin by the detergent fiber method [30]. Each determination was performed once for each of the three particle-size fractions from a single biosorbent preparation; values reported in Table S4 as mean ± SD across fractions are descriptive summaries only.

The point of zero charge (pH_{PZC}) was determined for each of the three particle-size fractions (75, 150, and 300 μm) of both NC and CT using the batch equilibrium method [31,32]. A 0.4 g portion of biosorbent was added to 80 mL of 0.05 M KNO_3, the initial pH was adjusted between 2 and 11 with 0.1 M HCl or NaOH, and after 24 h equilibration at 200 rpm the final pH was recorded. The pH_{PZC} was taken as the intersection of the pH_{final} versus pHinitial curve with the line $pH_{final} = pH_{initial}$. Six pH_{PZC} drift curves, corresponding to NC and CT at each particle size, are presented in Fig. S3.

2.4. Batch sorption experiments

2.4.1. Stock solution preparation

Individual metal solutions ($C_o = 50$ mg L^{-1}) of As(V), Cd(II), and Pb(II) were prepared from 1000 mg L^{-1} certified standards (H_3AsO_4, $Cd(NO_3)_2$, $Pb(NO_3)_2$; analytical grade, Merck). The initial concentration was selected as representative of moderately contaminated industrial effluents (electroplating, battery manufacturing, mining). Solution pH was controlled using 0.1 M citrate buffers (citric acid/sodium citrate) for pH 4.0 and 6.0, 0.1 M phosphate buffers (KH_2PO_4/Na_2HPO_4) for pH 6.8 and 8.0, and a borate buffer (0.2 M H_3BO_3 + 0.2 M NaOH, with KCl) for pH 8.5. The ionic strength was not independently adjusted to a common value across buffers; therefore, it varied implicitly according to the buffer system used at each pH. The use of different buffer identities across pH levels (citrate, phosphate, borate) introduces a potential confound between pH and buffer chemistry. This is particularly relevant at pH 6.8 and 8.0, where phosphate is tetrahedrally isoelectronic with arsenate and can compete for oxyanion sorption sites on oxygen-functionalized surfaces, and where phosphate can also form insoluble lead phosphate phases ($Pb_3(PO_4)_2$). Citrate may chelate divalent cations (log K ≈ 3.8 for Cd^{2+} and ≈ 4.1 for Pb^{2+}; [33]) and may also coordinate with As(V) at pH 4.0, although with markedly lower affinity than for divalent cations. The implications of buffer identity for the interpretation of pH effects on all three contaminants are discussed in Section 4.1.

2.4.2. Effect of pH and particle size

A 5 × 3 full factorial design with two independent replicates per cell ($n = 30$ per metal) was used to evaluate the effects of pH (4.0, 6.0, 6.8, 8.0, and 8.5) and particle size (75, 150, and 300 μm) at a fixed biosorbent dosage of 10 g L^{-1}. The initial pH was controlled using 0.1 M citrate buffer for pH 4.0 and 6.0, 0.1 M phosphate buffer for pH 6.8 and 8.0, and borate buffer prepared from 0.2 M H_3BO_3 and 0.2 M NaOH for pH 8.5. Ionic strength was not independently adjusted to a common background electrolyte concentration and therefore varied implicitly among buffer systems. Aliquots of 50 mL were agitated at 200 rpm for 24 h at 20 ± 2 °C, then filtered under vacuum and analyzed by ICP-OES (Section 2.7).

2.4.3. Effect of biosorbent dosage and particle size

A 3 × 3 full factorial design with two independent replicates per cell ($n = 18$ per metal) was used to evaluate the effects of biosorbent dosage (5, 10, and 15 g L^{-1}) and particle size (75, 150, and 300 μm) at the apparent optimal pH identified for each contaminant in Section 2.4.2: pH 4.0 for As(V), pH 6.0 for Cd(II), and pH 8.5 for Pb(II). The corresponding buffer systems were 0.1 M citrate buffer for As(V) at pH 4.0, 0.1 M citrate buffer for Cd(II) at pH 6.0, and borate buffer prepared from 0.2 M H_3BO_3 and 0.2 M NaOH for Pb(II) at pH 8.5. Other experimental conditions were as described in Section 2.4.2.

2.5. Adsorption kinetics and equilibrium uptake

Kinetic experiments were performed in duplicate (50 mL solution; biosorbent dosage 15 g L^{-1}; 200 rpm; 20 ± 2 °C) at the apparent optimal pH and particle size identified for each contaminant in Section 2.4.2: 150 μm at pH 4.0 for As(V); 75 μm at pH 6.0 for Cd(II); 150 μm at pH 8.5 for Pb(II). The corresponding buffer systems were 0.1 M citrate buffer for As(V) at pH 4.0, 0.1 M citrate buffer for Cd(II) at pH 6.0, and borate buffer prepared from 0.2 M H_3BO_3 and 0.2 M NaOH for Pb(II) at pH 8.5; ionic strength was not independently adjusted to a common background electrolyte concentration and therefore varied implicitly according to the buffer system. Aliquots were withdrawn at 0, 10, 40, 70, 130, 190, and 250 min, filtered, and analyzed by ICP-OES. Pseudo-first-order (PFO), pseudo-second-order (PSO), and intraparticle diffusion (Weber–Morris, IPD) models were fitted to the kinetic data; model expressions and parameter definitions are compiled in Table S2. PFO and PSO were fitted by non-linear regression (Levenberg–Marquardt algorithm); IPD by ordinary least-squares of qt versus t0.5. IPD was used to identify rate-controlling stages compatible with diffusion-limited transport rather than as exclusive mechanistic evidence. Model adequacy was evaluated using R^2, R^2adj, RMSE, and χ^2 [34,35].

Equilibrium uptake experiments were conducted for 250 min, corresponding to the maximum contact time used in the kinetic assays and selected to allow direct comparison between kinetic and equilibrium datasets. Three biosorbent dosages (5, 10, and 15 g L^{-1}) were evaluated under the apparent optimal conditions identified for each contaminant in Section 2.4.2. Because this contact time represents an operational endpoint rather than a full 24 h equilibration period, the resulting values are interpreted as apparent equilibrium uptake under the tested conditions. The same buffer systems used in the dosage–particle-size assays (Section 2.4.3) were applied: 0.1 M citrate buffer for As(V) at pH 4.0, 0.1 M citrate buffer for Cd(II) at pH 6.0, and borate buffer prepared from 0.2 M H_3BO_3 and 0.2 M NaOH for Pb(II) at pH 8.5; ionic strength was not independently adjusted to a common background electrolyte concentration and therefore varied implicitly according to the buffer system. Because a single initial concentration ($C_o = 50$ mg L^{-1}) combined with three dosages produces narrow equilibrium concentration ranges unsuitable for reliable isotherm regression, results are reported as apparent uptake values rather than as Langmuir or Freundlich parameters, and no maximum adsorption capacity (qmax) is reported. The combination of kinetic and apparent-equilibrium series at the same dose range (5–15 g L^{-1}) and metal-specific optima allows direct evaluation of dose dependence and time-to-equilibrium across contaminants; the resulting inter-series comparison for Cd(II) is examined in Sections 3.3 and 4.1. This isotherm limitation is discussed further in Section 4.4.

2.6. Fixed-bed column experiments

Continuous-flow experiments were conducted in duplicate for each contaminant (two independent column runs per metal) in a glass column (internal diameter 2.5 cm; total height 35 cm) packed with CT biosorbent at a single particle size of 300 μm, coarser than the batch optimum for any metal and selected to minimize pressure drop. A glass-wool plug (≈ 2 cm) retained the biosorbent; packed mass was 6 g (bed height 9.5–10 cm; Table S5). Metal solutions ($C_o = 50$ mg L^{-1}) were pumped in down-flow mode at 4 mL min^{-1}, corresponding to an empty bed contact time (EBCT) of ≈ 11.7–12.3 min. Column experiments were conducted using the same contaminant-specific pH and buffer systems applied in the kinetic and apparent-equilibrium assays: 0.1 M citrate buffer for As(V) at pH 4.0, 0.1 M citrate buffer for Cd(II) at pH 6.0, and borate buffer prepared from 0.2 M H_3BO_3 and 0.2 M NaOH for Pb(II) at pH 8.5. The column was conditioned with 100 mL of the corresponding pH buffer prior to operation. Effluent was sampled at 10, 40, 70, 130, 190, and 250 min and analyzed by ICP-OES.

Breakthrough curves (C/C_o versus t) were fitted to the Thomas model by non-linear regression using the Levenberg–Marquardt algorithm as implemented in scipy.optimize.curve_fit [36,37]. The mathematically equivalent Yoon–Nelson parameters were derived algebraically ($K_{YN} = K_{TH} \times C_o$; $\tau = q_o \cdot m / (Q \cdot C_o)$) [38]. Goodness of fit was evaluated using R^2 and χ^2. Equations and parameter definitions are provided in Table S2. The Thomas model parameter q_o was interpreted as a model-derived bed capacity under the specific column operating conditions tested, rather than as an intrinsic maximum adsorption capacity of the biosorbent.

2.7. Metal analysis and statistical analysis

Residual metal concentrations in batch and column effluents were determined by inductively coupled plasma optical emission spectrometry (ICP-OES) according to ISO 11885:2007 at CERPER S.A. (Arequipa, Peru; INACAL-accredited, Reg. No. LE-003). Limits of detection were 0.02 mg L^{-1} for As, 0.001 mg L^{-1} for Cd, and 0.007 mg L^{-1} for Pb. Laboratory-fortified blank recoveries were 90–99%. Removal (%) = $[(C_o - Ce) / C_o] \times 100$, and qe (mg g^{-1}) = $[(C_o - Ce) \times V] / m$.

The effects of pH, particle size, and dosage on batch removal efficiency were evaluated using factorial ANOVA (Type II sums of squares) followed by Tukey's HSD ($\alpha = 0.05$). Effect size was quantified by partial eta-squared (η^2p), with 90% confidence intervals obtained by non-centrality inversion of the F statistic [39]; partial omega-squared (ω^2p) was reported in parallel as a less upwardly biased complement [40]. Effect-size interpretation followed Richardson [41]: $\eta^2p < 0.06$ = negligible; 0.06–0.14 = small; 0.14–0.60 = moderate; ≥ 0.60 = large. Analyses were performed in Python 3.12.3 using statsmodels 0.14 and SciPy 1.17.0, and cross-checked in R 4.5.1 [42] using the apaTables package [43]. The full ANOVA output (sums of squares, mean squares, F statistics) and the reproducible R and Python analysis scripts are openly available through the Zenodo repository deposit (DOI: https://doi.org/10.5281/zenodo.19646178; see Data availability). The limited factorial replication ($n = 2$ per cell) restricts the precision of effect-size estimation, particularly for Pb(II) (discussed further in Section 4.8). Figures were prepared in Origin 2021b.

3. Results

3.1. Effect of NaOH modification on surface chemistry

NaOH treatment produced a consistent pattern of physicochemical changes relevant to sorption performance. The point of zero charge (pH_{PZC}) was determined from the intersection of pH drift curves with the pHi = pHf bisector (Fig. S3a–c). For the native biosorbent (NC), pH_{PZC} was 4.47 ± 0.15 (mean ± SD, $n = 3$ particle-size fractions; range 4.31–4.60); after NaOH treatment (CT), pH_{PZC} increased to 6.83 ± 0.15 (range 6.71–7.00), corresponding to a net shift of 2.36 pH units (Fig. S3d). The low inter-size variability (CV < 3%) indicates that pH_{PZC} is governed by cell-wall composition rather than particle size within the 75–300 μm range. This shift is the most diagnostic change for charge-dependent behavior, because it reverses the expected direction of surface charge at the near-neutral pH values representative of many contaminated effluents.

FTIR spectra (Fig. 2; band assignments in Table S3) provided direct spectroscopic evidence of the chemical transformations underlying the pH_{PZC} shift. Spectra of NC, CT, and DA (after Pb(II) sorption) shared a broad O–H/N–H stretching band (3335–3340 cm^{-1}) and C—H stretching bands (2883–2884 cm^{-1}). The most diagnostic change was the disappearance of the C═O stretching band at ~1735 cm^{-1} (acetyl and uronic ester groups in hemicellulose), present only in NC and consistent with ester-bond saponification during alkaline treatment. Three fingerprint bands showed increased intensity in CT and DA relative to NC: the aromatic skeletal vibration at 1594 cm^{-1}, the C—H symmetric bending band at 1379 cm^{-1}, and the C—O stretching/C–O–C deformation band at 1028–1032 cm^{-1}. The β-glycosidic linkage band at 896 cm^{-1} became more pronounced after NaOH treatment. The CT and DA spectra showed minimal differences, indicating that Pb(II) sorption did not introduce new FTIR-detectable bands at the sensitivity of the measurement.

Compositional and textural analyses were consistent with these spectroscopic observations. NaOH treatment reduced hemicellulose from 18.2% to 12.4% and lignin from 22.8% to 19.5%, while cellulose increased in relative abundance from 28.5% to 32.1% (Table S4), consistent with partial hemicellulose solubilization and modest lignin loss during alkaline hydrolysis. Mean ash content increased from 0.72% in NC to 1.51% in CT ($\Delta \approx +109\%$), whereas phosphorus decreased from a mean of 49.3 mg kg^{-1} in NC to below detection in CT. Fe and Ca + Mg remained within comparable ranges in NC and CT. Because values correspond to single determinations for three particle-size fractions from a single biosorbent preparation, they are presented as descriptive observations rather than as the outcome of formal statistical testing (see Section 4.8 for further discussion). BET analysis (Table S6) showed that NaOH treatment reduced the specific surface area from 1.25 to 0.20 m^2 g^{-1} while increasing the average pore diameter from 1.88 nm (micropore range) to 7.98 nm (mesopore range, IUPAC); because BET reflects N_2 accessibility in the dry state, it may underestimate the sorption-relevant surface available in aqueous media (discussed mechanistically in Section 4.1). SEM (Fig. 1) revealed a compact, laminar NC surface with parallel ridges; CT showed surface disruption and exposure of regularly aligned pit-like features consistent with partial removal of surface-associated components; and DA showed locally smoother domains with a discrete bright deposit visible at higher magnification, consistent with adsorbed material at the outer surface.

3.2. Batch performance: Optimal conditions for each metal

Two independent factorial experiments were conducted: pH × particle size (5×3, $n = 30$; fixed dosage 10 g L^{-1}) and dosage × particle size (3×3, $n = 18$; at the metal-specific optimum pH identified from the first experiment). In the pH × particle-size experiment (Table 1a), all three predictors significantly affected Pb(II) and Cd(II) removal. For Pb(II), all predictors reached near-unity effect sizes (pH × particle-size interaction $\eta^2p = 0.999$; pH $\eta^2p = 0.997$; particle size $\eta^2p = 0.984$). For Cd(II), pH exerted a very large effect ($\eta^2p = 0.951$), particle size a large effect ($\eta^2p = 0.738$), and the interaction represented the strongest contribution ($\eta^2p = 0.979$). Removal of both cationic metals increased above the pHPZC of CT, with Pb(II) reaching 99.57 ± 0.19% at pH 8.5 and Cd(II) reaching 38.4 ± 0.9% at pH 6.0/75 μm (Fig. S1; further inter-series comparison in Section 3.3). For As(V), no main effect or interaction reached statistical significance (all $p > 0.05$; $\eta^2p < 0.08$), consistent with the negligible removal (<8%) observed across all 15 factor combinations.

The dosage × particle-size experiment (Table 1b; Fig. S2) confirmed that increasing biosorbent dosage from 5 to 15 g L^{-1} enhanced both Pb(II) and Cd(II) removal. For Cd(II), biosorbent dosage was the most influential factor ($\eta^2p = 0.991$; $F(2,9) = 518.6$, $p < 0.001$), with removal for the 75 μm fraction increasing from ~31% at 5 g L^{-1} to 76% at 10 g L^{-1} and 99.72 ± 0.01% at 15 g L^{-1}. For Pb(II), all predictors showed near-unity effect sizes ($\eta^2p \geq 0.998$), reflecting that >98% removal was already achieved at the lowest dosage. As(V) showed no significant response (all $p > 0.05$). The very high η^2p values for Pb(II) reflect the strong treatment effects combined with limited residual variance ($n = 2$ per cell) and should be interpreted as evidence of saturating effects (discussed further in Section 4.8). The optimal conditions are summarized in Table 2.

3.3. Reproducibility and dose dependence

The reproducibility of sorption performance across independent experimental series is central to the practical utility of a biosorbent for water treatment. This section compares Pb(II) and Cd(II) behavior across three independent series conducted at 15 g L^{-1}: the dosage × particle-size factorial (Section 3.2), the kinetic series at the metal-specific optimum, and the equilibrium series at three dosages. Pb(II) showed consistently high removal (>98.9%) across all three series, with qe decreasing monotonically from 9.96 ± 0.04 mg g^{-1} at 5 g L^{-1} to 3.33 ± 0.01 mg g^{-1} at 15 g L^{-1} in the equilibrium series (Table 3). Cd(II), in contrast, yielded markedly different outcomes across the four independent series conducted at nominally identical pH 6.0 and 75 μm: 99.72% removal in the dosage × particle-size factorial at 15 g L^{-1} (24 h contact), 38.4% removal in the pH × particle-size factorial at 10 g L^{-1} (24 h contact), and only 5.5–12.0% in the independent equilibrium series across 5, 10, and 15 g L^{-1} (250 min contact; qe = 0.35–0.55 mg g^{-1}; Table 3). A separate single-dose kinetic experiment at 15 g L^{-1} over 250 min reached $q_{e,exp.} = 3.36$ mg g^{-1} (≈ 100% removal; Table S7), in close agreement with the dosage × particle-size factorial result and confirming that Cd(II) approaches saturation when both biosorbent loading and contact time are sufficient. Operational details and inter-series variability are quantified in Table S9, and per-cell replicate dispersion (coefficients of variation) for both factorial designs is summarized in Table S11. For As(V), the equilibrium series yielded Ce consistently

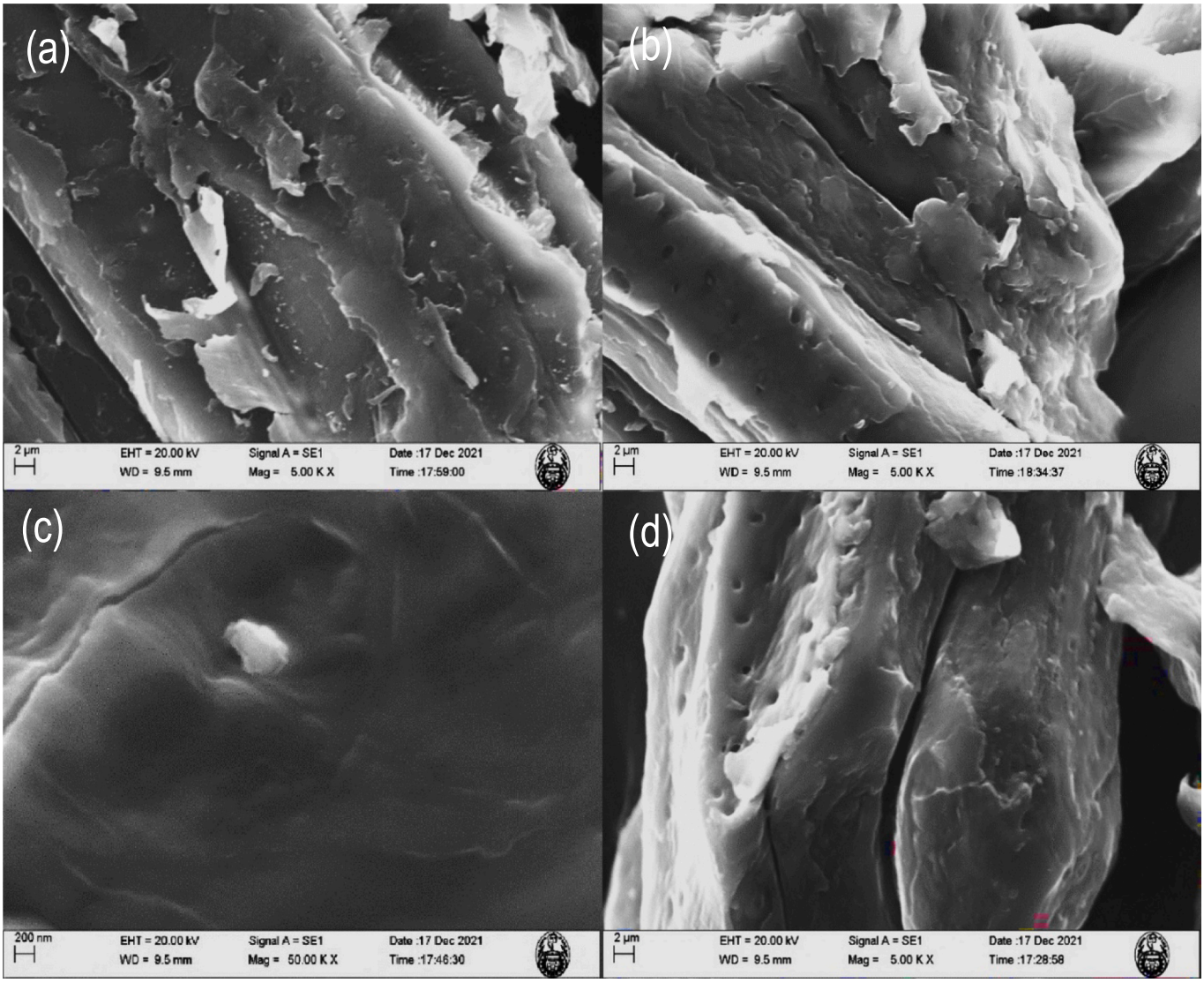


Fig. 1. SEM micrographs of olive stone (*Olea europaea* L.) at three processing stages: (a) native biosorbent (NC), 5.00 K×; (b) NaOH-modified biosorbent (CT), 5.00 K×; (c) post-adsorption biosorbent (DA) at high magnification (50.00 K×, 200 nm scale bar), showing a discrete surface deposit consistent with adsorbed Pb species; and (d) DA at 5.00 K× (2 µm scale bar), showing the corresponding overall textural appearance. Samples were mounted on aluminum stubs with carbon tape and examined without conductive coating using a Zeiss Supra 40 SEM operated at 20 kV with an SE1 detector and a working distance of 9.5 mm. NC = native biosorbent; CT = NaOH-modified; DA = CT after Pb(II) sorption.

exceeding C_0 at all three dosages (Table 3), reported as an empirical observation of poor and unstable retention; the implications are examined in Section 4.1.

Kinetic data (Table S7; Fig. 3) characterized the rate of approach to equilibrium under the optimal pH and particle-size conditions for each metal. Uptake was rapid during the initial phase; based on the fitted pseudo-first-order (PFO) model, more than 50% of the equilibrium capacity was attained within ~30 min for As(V) and ~ 60 min for Cd(II) and Pb(II). As(V) approached equilibrium after ~130 min ($k_1 = 0.0220$ min^{-1}); Cd(II) and Pb(II) required ~200 min ($k_1 = 0.0114$ and 0.0110 min^{-1}, respectively).

The PFO model provided the best overall fit for all three species based on combined R^2, R^2adj, RMSE, χ^2, AICc, and qe,calc/qe,exp. agreement. PFO-derived equilibrium capacities were 1.98 mg g^{-1} for As (V), 3.60 mg g^{-1} for Cd(II), and 3.76 mg g^{-1} for Pb(II), representing deviations of 4.0%, 7.2%, and 13.4% from experimental values. For Cd (II), PFO and PSO were statistically indistinguishable by AICc (ΔAICc = 1.45); PFO was retained based on superior qe,calc/qe,exp. agreement (PSO overestimated Cd(II) qe by 42%: 4.78 vs. 3.36 mg g^{-1}). The intraparticle diffusion model showed the poorest fit for As(V) (R^2 = 0.749) and Pb(II) (R^2 = 0.937), with qt versus $t^{0.5}$ plots displaying multilinearity rather than a single linear segment (Fig. 3c), and residuals of the PFO fits showed random scatter within the ±RMSE band (Fig. 3d). As discussed in Section 4.4, kinetic-model identity alone is not used here to infer mechanism.

The Cd(II) inter-series discrepancy (99.72% vs. 38.4% vs. 5.5–12.0%) represents a notable reproducibility limitation and cannot be attributed to a single factor. The series were conducted under nominally identical citrate buffering (pH 6.0) and used CT material from a single NaOH-modification preparation (Section 2.2), but differed in biosorbent dosage (10 vs. 15 g L^{-1}), contact time (250 min vs. 24 h), and replication regime; candidate contributing factors therefore include incomplete equilibration, dose-dependent saturation thresholds, and buffer-mediated complexation rather than batch-to-batch variability. By contrast, Pb(II) removal was internally consistent across series despite the same operational differences, indicating that Pb(II) is intrinsically less sensitive than Cd(II) to these variables. The mechanistic interpretation and practical implications are examined in Sections 4.1 and 4.2,

Table 1
Two-way ANOVA results (Type II SS) for apparent removal of Pb(II), Cd(II), and As(V) by NaOH-modified olive stone.

Predictor	Contaminant	df	F	p	η^2p	90% CI	ω^2p	Sig.
(a) pH × particle size factorial design (5 × 3; n = 30 per contaminant; residual df = 15)								
pH	Pb(II)	4	1070.39	<0.001	0.997	[0.990, 0.997]	0.995	***
pH	Cd(II)	4	73.57	<0.001	0.951	[0.869, 0.961]	0.936	***
pH	As(V)	4	0.328	0.855	0.080	[0.000, 0.122]	0.000	ns
Particle size	Pb(II)	2	465.51	<0.001	0.984	[0.961, 0.989]	0.981	***
Particle size	Cd(II)	2	21.17	<0.001	0.738	[0.442, 0.815]	0.691	***
Particle size	As(V)	2	0.121	0.887	0.016	[0.000, 0.089]	0.000	ns
pH × Size	Pb(II)	8	1641.40	<0.001	0.999	[0.996, 0.999]	0.998	***
pH × Size	Cd(II)	8	86.24	<0.001	0.979	[0.930, 0.980]	0.966	***
pH × Size	As(V)	8	0.131	0.997	0.065	[0.000, <0.001]	0.000	ns
(b) Dose × particle size factorial design (3 × 3; n = 18 per contaminant; residual df = 9)								
Dose	Pb(II)	2	2682.39	<0.001	0.998	[0.994, 0.999]	0.998	***
Dose	Cd(II)	2	518.59	<0.001	0.991	[0.969, 0.994]	0.989	***
Dose	As(V)	2	0.988	0.409	0.180	[0.000, 0.404]	0.000	ns
Particle size	Pb(II)	2	3863.15	<0.001	0.999	[0.996, 0.999]	0.998	***
Particle size	Cd(II)	2	89.85	<0.001	0.952	[0.836, 0.966]	0.937	***
Particle size	As(V)	2	0.655	0.542	0.127	[0.000, 0.345]	0.000	ns
Dose × particle size	Pb(II)	4	2262.50	<0.001	0.999	[0.996, 0.999]	0.998	***
Dose × particle size	Cd(II)	4	16.32	<0.001	0.879	[0.551, 0.902]	0.814	***
Dose × particle size	As(V)	4	1.547	0.269	0.407	[0.000, 0.517]	0.135	ns

Note. Effect sizes are reported as partial eta-squared (η^2p) with 90% confidence intervals estimated by noncentrality inversion of the F statistic [39], and as partial omega-squared (ω^2p) [40]. Effect-size interpretation followed the thresholds described in the Statistical analysis section. For non-significant effects with F < 1, noncentrality-based CIs may collapse to a near-zero upper bound, shown here as <0.001 — a computational artifact. For Pb(II), η^2p values approaching unity reflect saturating removal under limited residual variance. ***p < 0.001; ns = not significant at α = 0.05. Complete ANOVA outputs and reproducible analysis scripts are available in the Zenodo repository (DOI: https://doi.org/10.5281/zenodo.19646178).

Table 2
Best-performing factorial conditions for apparent removal of Pb(II), Cd(II), and As(V) by NaOH-modified olive stone.

Contaminant	pH	Particle size (μm)	Dosage (g L^{-1})	Removal (%)	Tukey group	Optimizing factorial design
Pb(II)	8.5 [b]	150	10	99.57 ± 0.19	A	pH × Size
Cd(II)	6.0	75	15	99.72 ± 0.01 [a]	A	Dose × Size
As(V)	4.0	150	15	7.30 ± 1.75	A	None (n.s.)

Note. Conditions: C_o = 50 mg L^{-1}, 24 h, 20 ± 2 °C, 200 rpm, and n = 2 per cell. Optimal levels were selected by Tukey's HSD as the highest cell mean within Group A (α = 0.05). The "Optimizing factorial design" column indicates the factorial experiment from which the reported condition was obtained (Table 1). For As(V), no factor reached significance in either factorial design; therefore, the listed conditions correspond to the highest observed mean. n.s. = not significant. [a] The 99.72% Cd(II) value represents the upper bound of an operational range (5.5–99.7% across independent series; Table 3, Table S9), largely attributable to operational differences between series (dose, contact time, replication regime); see Sections 2.2 and 4.1 for the single-batch design caveat. [b] The Pb(II) optimum was identified at pH 8.5 using borate buffer and is therefore not subject to the phosphate-mediated confound discussed for Pb(II) removal at pH 6.8–8.0 (Sections 4.1 and 4.8).

respectively.

3.4. Fixed-bed column performance

Fixed-bed column experiments were conducted under a common set of operating conditions (C_o = 50 mg L^{-1}; Q = 4 mL min^{-1}; m = 6 g; bed height 9.5–10 cm; particle size 300 μm; EBCT ≈ 12 min; full conditions in Table S5) to evaluate the dynamic performance of NaOH-modified olive stone for the three contaminants under continuous-flow operation representative of practical water treatment. The coarse particle size (300 μm), selected to minimize pressure drop, is coarser than the batch-identified optimum for any of the three metals; the implications for batch–column comparison are examined in Section 4.3.

Breakthrough curves (Fig. 4) showed the characteristic S-shaped profile, with As(V) breaking through earliest, followed by Pb(II) and Cd (II). As(V) and Pb(II) approached $C/C_o \approx 1.0$ within 250 min, whereas the Cd(II) curve did not reach full saturation ($C/C_o \approx 0.87$ at 250 min). Both Thomas and Yoon–Nelson parameterizations yielded $R^2 > 0.97$ for all three species, with Pb(II) showing the best fit ($R^2 = 0.994$; Table 4). The 50% breakthrough time (τ) followed As(V) (53.0 min) < Pb(II) (68.1 min) < Cd(II) (120.3 min), and model-derived column capacities (q_o) followed Cd(II) (4.01 mg g^{-1}) > Pb(II) (2.27 mg g^{-1}) > As(V) (1.77 mg g^{-1}).

The Thomas rate constant was markedly higher for Pb(II) (0.004156 L mg^{-1} min^{-1}) than for As(V) (0.000926) and Cd(II) (0.000883), indicating faster column kinetics for Pb(II) consistent with the shorter τ and the steeper breakthrough curve observed in Fig. 4.

Two caveats constrain the interpretation of the column results. First, the Cd(II) fitted parameters (q_o = 4.01 mg g^{-1}, K_{TH} = 0.000883 L mg^{-1} min^{-1}, τ = 120.3 min) derive from a breakthrough curve that did not reach saturation within the 250-min operating window, and therefore represent model extrapolations rather than observed equilibria. Second, the numerical q_o reported for As(V) (1.77 mg g^{-1}) exceeds the negligible batch uptake of the same contaminant (Section 3.3); this reflects that continuous-flow operation integrates transient retention along the breakthrough curve rather than allowing bulk re-equilibration, and the rapid breakthrough (τ = 53.0 min) confirms that As(V) retention remains limited under both operational modes, consistent with the absent net adsorption observed in batch equilibrium ($C_e > C_o$; Section 3.3 and Table 3). These caveats are examined further in Section 4.3.

3.5. Charge-dependent behavior in batch and continuous flow

The combined batch and fixed-bed datasets reveal a consistent pattern of charge-dependent removal that differentiates the three contaminants and the two operational modes. Three observations summarize this pattern.

First, Pb(II) showed robust and reproducible removal across all experimental configurations. Batch removal remained above 98.9% across all three independent series tested at 15 g L^{-1} (factorial optimum,

Table 3
Observed equilibrium concentrations, apparent uptake, and removal of Pb(II), Cd(II), and As(V) by NaOH-modified olive stone at three biosorbent doses (C_o = 50 mg L^{-1}).

Dose (g L^{-1})	Contaminant	C_e (mg L^{-1})	q_e (mg g^{-1})	Removal (%)
5	Pb(II)	0.22 ± 0.20	9.96 ± 0.04	99.6
5	Cd(II)	47.23 ± 0.50	0.55 ± 0.10	5.5
5	As(V)	52.60 ± 1.76 [a]	n.d.	n.d.
10	Pb(II)	0.53 ± 0.60	4.95 ± 0.06	98.9
10	Cd(II)	46.50 ± 0.26	0.35 ± 0.03	7.0
10	As(V)	53.83 ± 0.66 [a]	n.d.	n.d.
15	Pb(II)	0.05 ± 0.07	3.33 ± 0.01	99.9
15	Cd(II)	44.00 ± 0.26	0.40 ± 0.02	12.0
15	As(V)	51.57 ± 1.35 [a]	n.d.	n.d.

Note. Ce = equilibrium concentration; q_e = apparent amount adsorbed at equilibrium; n.d. = not determined because no net adsorption was detected. Values are mean ± SD (n = 3). Conditions: C_o = 50 mg L^{-1}, contact time = 250 min, 20 ± 2 °C, 200 rpm, and contaminant-specific optimal pH and particle size (Table 2). For Cd(II), the values shown correspond to the dose-dependent equilibrium series, which falls 6–8-fold below the kinetic and factorial series performed under identical pH and particle size and is treated as a localized reproducibility outlier (Section 4.1; Table S9); representative Cd(II) uptake is better reflected by the kinetic series ($q_e \approx 3.36$ mg g^{-1}). [a] For As(V), Ce exceeded C_o at all doses, indicating no net adsorption under these equilibrium conditions; therefore, qe and removal were not calculated. Future work should include blank leaching controls using CT in contaminant-free buffered solutions to verify whether this pattern reflects matrix effects or apparent release from the biosorbent (Section 4.8).

Table 4
Thomas and Yoon–Nelson model parameters fitted to fixed-bed breakthrough curves of Pb(II), Cd(II), and As(V) using NaOH-modified olive stone.

Contaminant	K_{TH} (L mg^{-1} min^{-1})	q_0 (mg g^{-1})	K_{YN} (min^{-1})	τ (min)	R^2	χ^2
Pb(II)	0.004156	2.27	0.2078	68.1	0.994	0.006
Cd(II)	0.000883 [a]	4.01 [a]	0.0441 [a]	120.3 [a]	0.972	0.071
As(V)	0.000926	1.77 [b]	0.0463	53.0 [b]	0.977	0.088

Note. K_{TH} = Thomas rate constant; q_0 = Thomas model-estimated column adsorption capacity; K_{YN} = Yoon–Nelson rate constant; τ = time required for 50% breakthrough. Conditions: C_o = 50 mg L^{-1}, Q = 4 mL min^{-1}, m = 6 g, bed height = 9.5–10 cm, and particle size = 300 μm. Thomas parameters were fitted by non-linear regression using the Levenberg–Marquardt algorithm. Yoon–Nelson parameters were derived algebraically from the Thomas model using $K_{YN} = K_{TH} \times C_o$ and $\tau = q_e m/(QC_o)$. [a] The Cd(II) breakthrough curve did not reach complete saturation within the experimental runtime ($C/C_o \approx 0.87$ at 250 min); therefore, the corresponding parameters represent model-based extrapolations and should be interpreted with caution. [b] The numerical q_0 value for As(V) reflects transient retention integrated along the breakthrough curve rather than process-relevant adsorption capacity; the rapid breakthrough (τ = 53.0 min) indicates limited arsenate retention under continuous-flow operation (Section 4.3).

kinetic series, equilibrium series; Sections 3.2 and 3.3), and column operation yielded a clean S-shaped breakthrough with $R^2 = 0.994$ and a well-defined dynamic operation time of τ = 68.1 min (Section 3.4). Removal exceeded 98% already at the lowest dosage tested (5 g L^{-1}), indicating that operating conditions were not limiting under the regime tested.

Second, Cd(II) showed uptake that was strongly condition-dependent and operationally sensitive. Batch removal spanned from 5.5 to 12.0% in the equilibrium series to 99.72% in the dosage × particle-size factorial under nominally identical pH, both conducted using CT material from a single NaOH-modification preparation (Section 2.2) under different operational conditions (dosage, contact time, and replication regime; Section 3.3). In column operation, Cd(II) showed the latest breakthrough among the three metals (τ = 120.3 min), the highest fitted column capacity (q_0 = 4.01 mg g^{-1}), and an incomplete approach to saturation at 250 min. The combination of strong dosage dependence, inter-series variability, and extrapolated column parameters indicates that Cd(II) performance is operationally usable but requires standardized operating conditions (dosage and contact time) for reproducibility.

Third, As(V) showed consistently limited removal across all configurations. Batch removal remained below 8% across the 15 pH × size combinations and the 9 dosage × size combinations tested, with Ce exceeding C_o at all three dosages in the equilibrium series (Section 3.3). Column operation yielded the earliest breakthrough (τ = 53.0 min) and the lowest column capacity (q_0 = 1.77 mg g^{-1}). No operating condition within the tested parameter space yielded As(V) removal compatible with water treatment application.

Comparing batch and column ranking provides additional information for process design. Under batch operation at 15 g L^{-1}, Pb(II) yielded the highest uptake (qe up to 9.96 mg g^{-1} in the equilibrium series), while Cd(II) ranged from 0.40 to 3.36 mg g^{-1} across series. Under column operation at 6 g packed bed, Cd(II) yielded the highest fitted q_0 (4.01 mg g^{-1}). This apparent inversion reflects the different operational regimes (different biosorbent mass, different particle size, and for Cd(II) an incomplete saturation at the end of the run) rather than a reversal of intrinsic affinity; the mechanistic interpretation is developed in Section 4.1, and the operational implications for process design are examined in Section 4.3. Fig. 5 summarizes the charge-dependent performance pattern across both operational modes.

4. Discussion

4.1. Mechanistic basis of charge-dependent performance

NaOH treatment altered the biosorbent surface through several interconnected processes that together explain the charge-dependent performance observed in both batch and fixed-bed configurations. Alkaline hydrolysis produced compositional shifts consistent with hemicellulose solubilization and modest lignin loss (hemicellulose 18.2% → 12.4%, lignin 22.8% → 19.5%, cellulose 28.5% → 32.1%; Table S4), consistent with reports on alkaline pretreatment of lignocellulosic residues [16,17,44]. BET surface area decreased from 1.25 to 0.20 m^2 g^{-1} but average pore diameter increased from 1.88 to 7.98 nm (Table S6), indicating reduced contribution of the smallest pores and greater accessibility of larger domains; similar textural modifications have been reported for olive-derived materials [29]. FTIR (Fig. 2; Table S3) provided direct spectroscopic evidence of ester-bond saponification at ~1735 cm^{-1}, consistent with the formation of carboxylate salts analogous to those reported for NaOH-treated pineapple waste biomass [45]. Intensification of the aromatic band at 1594 cm^{-1}, the C–O/C–O–C deformation at 1028–1032 cm^{-1}, and the β-glycosidic linkage at 896 cm^{-1} in CT and DA is consistent with a greater relative contribution of lignin- and cellulose-dominated domains after hemicellulose removal. The minimal spectral difference between CT and DA indicates that Pb(II) sorption did not introduce new FTIR-detectable bands, consistent with a mechanism dominated by electrostatic interactions and ion exchange on pre-existing carboxylate- and hydroxyl-containing surface domains.

The pH_{PZC} shift from 4.47 to 6.83 is the most consequential change for charge-dependent performance. The shift was essentially independent of particle size (CV < 3%; Fig. S3d), indicating that surface chemistry governing proton exchange is controlled by cell-wall composition rather than particle size. The upward shift is consistent with ester-bond saponification and greater exposure of hydroxyl-rich cellulose domains, both of which increase surface proton buffering capacity. For Pb(II), the optimum pH (8.5) lies clearly above the pH_{PZC}, favoring a net negative surface charge and therefore electrostatic attraction and complexation with deprotonated oxygen-containing groups; although partial $Pb(OH)^+$ hydrolysis becomes significant at this pH, bulk $Pb(OH)_2$ precipitation is thermodynamically favorable only above pH ≈ 9, so the observed uptake is consistent with sorption-

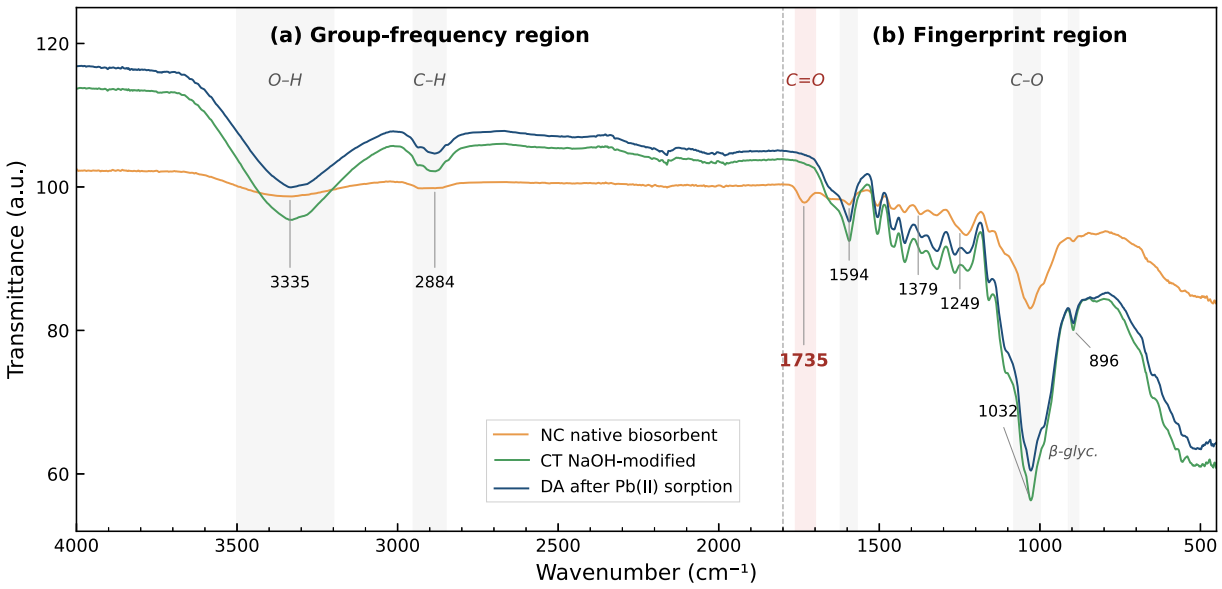


Fig. 2. FTIR transmittance spectra of olive stone (*Olea europaea* L.) at three processing stages: native biosorbent (NC, orange), NaOH-modified biosorbent (CT, green), and post-adsorption biosorbent (DA, blue) collected after Pb(II) sorption experiments. The spectra are shown for **(a)** the group-frequency region (4000–1800 cm^{-1}) and **(b)** the fingerprint region (1800–450 cm^{-1}). The band near 1735 cm^{-1} (highlighted), assigned to acetyl/uronic ester C═O stretching vibration of esterified hemicellulose, was observed in NC but is absent after NaOH treatment, consistent with alkaline saponification. The minimal spectral difference between CT and DA indicates that Pb(II) sorption did not introduce new FTIR-detectable bands at the sensitivity of the measurement, consistent with retention on pre-existing carboxylate- and hydroxyl-containing surface domains. Complete band assignments are provided in Table S3. Transmittance traces are vertically offset for clarity (arbitrary units). (For interpretation of the references to colour in this figure legend, the reader is referred to the web version of this article.)

dominated retention. A caveat applies to Pb(II) at pH 6.8 and 8.0, where phosphate in the buffer medium can form insoluble lead phosphate phases ($Pb_3(PO_4)_2$; log Ksp ≈ −43): the factorial optimum (pH 8.5, borate buffer) is not affected by this confound, but Pb(II) removal values at pH 6.8 and 8.0 must be interpreted as upper bounds that integrate sorption and possible phosphate-mediated precipitation contributions. The robustness of Pb(II) removal across all experimental series (>98.9%; Section 3.3) is consistent with strong intrinsic affinity for the deprotonated carboxylate and hydroxyl groups of the modified surface, and with interaction mechanisms previously reported for olive stone waste [46]. Distribution coefficients (Kd) derived from the dose-dependent series corroborate the markedly stronger affinity of the modified surface for Pb (II) than for Cd(II) (Table S10).

For Cd(II), the optimum pH (6.0) lies approximately 0.8 units below the mean pH_{PZC} of CT; under these near-neutral conditions, carboxyl groups (pKa ≈ 4–5) are expected to be largely deprotonated even though the surface is not yet net negative, indicating that electrostatic attraction alone is insufficient and that specific interactions with deprotonated carboxylate and surface hydroxyl groups likely contribute. The pronounced dosage effect ($\eta^2p = 0.991$) is the dominant and most reproducible driver of Cd(II) removal: within the dose × particle-size factorial, removal rises monotonically with dose at pH 6.0/75 μm (31% → 76% → 100% for 5 → 10 → 15 g L^{-1}; Section 3.2), placing the system on a steep sensitivity threshold near 10–15 g L^{-1}. Contact time is not the controlling factor under the tested conditions, because the kinetic series reached near-complete uptake within 250 min at 15 g L^{-1} (Section 3.3); citrate-mediated complexation at pH 6.0 (log K ≈ 3.8 for Cd^{2+}; [33]) is at most a secondary modulating factor and cannot account for the inter-series discrepancy, since all series shared nominally identical citrate buffering. Because CT material from a single NaOH-modification preparation was used throughout (Section 2.2), batch-to-batch variability is also ruled out as a contributor. The inter-series variability (99.72% vs. 38.4% vs. 5.5–12.0%; Section 3.3 and Table S9) therefore comprises two distinct components: a reproducible, dose-governed component captured within the dose × particle-size factorial, and a residual run-to-run component evident in the lower-than-predicted values of the pH × particle-size factorial cell and, most markedly, in the dose-dependent equilibrium series, which fell 6–8-fold below both the dose–time prediction and the kinetic series performed under identical conditions (15 g L^{-1}, 250 min). This residual is a localized, unresolved reproducibility limitation rather than a generalized instability. The implication is that Cd(II) performance is mechanistically feasible but operationally unstable without standardized operating conditions (dosage and contact time) and controlled replication (Section 4.8).

For As(V), the mechanistic picture is fundamentally different. Under the tested pH range, As(V) exists predominantly as anionic species ($H_2AsO_4^-$ at pH 2–7; $HAsO_4^{2-}$ at pH 7–11; [2,5]), and lignocellulosic biosorbents typically show poor affinity for these species [7]. Above the pH_{PZC} of CT (6.83), the net negative surface charge would be expected to repel arsenate, and NaOH treatment reinforces rather than alleviates this rejection. At pH 4.0 the surface should carry a net positive charge; the fact that As(V) removal nonetheless remained below 8% under these nominally favorable conditions indicates that factors beyond surface charge are operative. An electrostatically favorable surface charge is a necessary but not sufficient condition for oxyanion retention. Below the pH_{PZC} of the CT material (6.83), the integrated surface charge is net positive — operationally defined by the pH_{PZC} and reflecting suppressed carboxylate ionization together with protonation of minor basic sites rather than the generation of oxyanion-specific binding sites — and this would in principle promote the electrostatic approach of arsenate ions. However, the actual retention requires specific complexation with sorption sites of suitable chemistry. The functional groups generated and exposed by NaOH treatment — deprotonated carboxylate ($–COO^-$, pKa ≈ 4–5) and hydroxyl (–OH) — have high affinity for cationic metals through inner-sphere complexation [47] but low affinity for oxyanions, which require positively charged binding sites such as protonated amines, hydroxyl groups associated with hydrolyzed metal centers (Fe-OH, Al-OH, La-OH), or coordinatively unsaturated metal sites [7,15,48]. The low As(V) uptake at pH 4.0 therefore supports rather than contradicts the central hypothesis: NaOH modification favors cation-binding chemistry over oxyanion-binding chemistry, and electrostatic favorability cannot compensate for the absence of suitable sorption sites. This

is the mechanistic justification for the dual-modification strategy (NaOH followed by Fe(III) or La(III) impregnation) proposed as a future development pathway in Section 4.5.

A methodological consideration must be acknowledged: the pH × particle-size factorial employed different buffer systems across pH levels (citrate at pH 4.0 and 6.0; phosphate at pH 6.8 and 8.0; borate at pH 8.5). Phosphate is tetrahedrally isoelectronic with arsenate and a well-documented competitor for oxyanion sorption sites, with phosphate concentrations in the buffered treatments (several mM) substantially exceeding the As(V) concentration (50 mg L^{-1} ≈ 0.67 mM as As). Consequently, the null effect of pH on As(V) removal observed in the ANOVA cannot be cleanly attributed to surface-charge independence: the pH 6.8 and 8.0 treatments were subject to phosphate competition that may have overridden any residual electrostatic effect, whereas pH 4.0 (citrate) and pH 8.5 (borate) were not. The conservative interpretation is that As(V) removal remained poor across all three buffer windows tested, but the factorial design does not permit a clean test of pH as an independent variable for this analyte.

A second observation requiring caution is that Ce consistently exceeded C_0 for As(V) at all three biosorbent dosages (Table 3), a pattern interpreted cautiously as evidence of poor and unstable arsenate retention. Two compatible and non-exclusive working hypotheses may account for the observation: (i) the complete loss of phosphorus during NaOH treatment (49.3 mg kg^{-1} → below detection; Table S4) suggests dissolution of phosphate-bearing mineral phases, and because As and P share analogous geochemical behavior, trace As associated with these phases may have been redistributed and subsequently released under acidic conditions; (ii) citrate at pH 4.0 may have contributed to trace-element mobilization by complexing cationic components of the biosorbent matrix. Both are hypotheses only, as the mineralogical speciation of the biosorbent was not directly characterized. Regardless of the specific mechanism, the practical implication is clear: NaOH-modified olive stone is not effective for arsenate removal under the conditions tested.

4.2. Implications for water treatment process design

The mechanistic framework developed above translates into a clear set of implications for the design of water treatment systems using NaOH-modified olive stone. Rather than treating the biosorbent as a general-purpose material to be optimized, the more useful framing for process design is a contaminant-specific selection logic: the same alkaline modification that favors removal of cationic contaminants constrains the retention of anionic contaminants, so the material is appropriate for cation-dominated effluents and inappropriate for anion-dominated effluents, with mixed cation–anion effluents requiring either sequential treatment stages or dual-functionality materials. Fig. 5 visually summarizes this contaminant-specific performance across batch and fixed-bed operation, supporting the selection logic developed below.

For cation-dominated effluents, NaOH-modified olive stone is a viable treatment option for Pb(II). Removal exceeded 98.9% across all independent experimental series at dosages as low as 5 g L^{-1} (Section 3.3), indicating that the material is robust to reasonable variation in operating conditions within the tested envelope. Practical targets for Pb-contaminated effluents from electroplating, battery manufacturing, and mining — among the principal point sources in the southern Peruvian region where olive stone is locally available [21] — can be addressed with dosages within the tested range (5–15 g L^{-1}) at pH values above the pH_{PZC} of the modified material. The breakthrough behavior in fixed-bed operation ($\tau = 68.1$ min at $Q = 4$ mL min^{-1}, 6 g packed bed; Section 3.4) is consistent with this assessment and provides a baseline for scaling analyses.

For Cd(II), the situation is more nuanced and requires explicit process design considerations. Under optimized batch conditions, removal can reach 99.72%, but the observed inter-series variability (5.5–99.7%; Section 3.3) indicates that direct application of the optimized-factorial result to an operational design would be premature. Practical implementation would require: (i) standardized operational protocols (dosage and contact time) that control the inter-series variability observed across experimental series (Section 3.3); (ii) pre-implementation testing on the specific effluent of interest, since citrate-like complexing agents common in some industrial waters may reduce the free Cd^{2+} fraction available for sorption; and (iii) dose control above the operational threshold (≥ 15 g L^{-1} under the tested conditions) to ensure consistent performance. The operational envelope for Cd(II) is therefore narrower than for Pb(II), but the material remains usable within that envelope.

For anion-dominated effluents, and specifically for arsenate-containing waters, NaOH-modified olive stone is unsuitable. Removal below 8% across all tested conditions (Section 3.2) indicates that the modification direction (increased carboxylate and hydroxyl exposure, elevated pH_{PZC}) reinforces rather than alleviates the electrostatic barrier to arsenate retention. Alternative surface modifications that generate positively charged sorption sites are required. Metal-loaded biosorbents provide a demonstrated route: La(III)-loaded watermelon rind has achieved Langmuir qmax = 74.8 mg g^{-1} for As(V) [15] and Fe-impregnated henequen biochar qmax = 15.2 mg g^{-1} [48,57]. A sequential dual-modification strategy — NaOH modification followed by Fe(III) impregnation — may be a feasible route for combining cation- and anion-binding domains on a single material; however, the complete loss of phosphorus observed during NaOH treatment (Table S4) indicates disruption of mineral phases whose effect on exogenous Fe(III) retention is not yet known and requires direct experimental testing.

For mixed cation–anion effluents — which represent many real industrial and mining wastewaters — the charge-dependent performance pattern documented here implies that a single alkaline-modified material is insufficient. Treatment configurations that combine NaOH-modified olive stone (for cation removal) with a metal-loaded biosorbent (for anion removal) in sequential fixed-bed columns, or that develop bifunctional materials through combined modification, are more promising design directions than further optimization of a single alkaline treatment. The valorization of olive stone as a functional biosorbent aligns these treatment choices with circular-economy principles, given the large quantities of the residue generated in olive-producing regions globally and locally [20,21].

4.3. Batch vs fixed-bed: Operational considerations

The comparison between batch and fixed-bed results provides operational information that is critical for process design but is often absent from adsorption studies that report only one operational mode. Three observations emerge from the parallel evaluation conducted here, and each has specific implications for the scaling of NaOH-modified olive stone as a treatment material.

First, the ranking of model-derived fitted column capacities (q_0: Cd > Pb > As; Section 3.4) differs from the ranking of batch uptake under the equilibrium series (qe: Pb > > Cd > As; Section 3.3). This apparent inversion between the two operational modes should not be interpreted as a reversal of intrinsic affinity, but rather as a consequence of the different experimental conditions applied: the column used a single coarse particle size (300 μm, selected to minimize pressure drop), whereas batch experiments used metal-specific optima (75 μm for Cd (II); 150 μm for As(V) and Pb(II)). This alters intraparticle diffusion distances and limits direct numerical comparison between the two datasets. Batch and column systems also probe different aspects of sorption performance — equilibrium under finite contact time versus dynamic breakthrough over time — and column operation is more sensitive to sorption sites with slower access kinetics [26]. The practical implication is that column-based scaling estimates for a given metal cannot be derived directly from batch qe values of the same metal under different particle-size conditions; independent column characterization at the target particle size is required.

Second, the incomplete saturation of the Cd(II) breakthrough curve

($C/C_o \approx 0.87$ at 250 min) means that the fitted Cd(II) parameters (q_o = 4.01 mg g^{-1}, K_{TH} = 0.000883 L mg^{-1} min^{-1}, τ = 120.3 min) represent model extrapolations beyond the observed data range. Longer operation times (e.g., to $C/C_o \geq 0.95$) would be required to verify these values under the same operating conditions, and this should be considered explicitly in any scaling calculation based on the reported Cd(II) q_o. The Pb(II) and As(V) curves, by contrast, reached near-complete saturation within the 250-min window (Fig. 4), and their fitted parameters can be interpreted with greater confidence.

Third, the modest numerical q_o reported for As(V) (1.77 mg g^{-1}) exceeds the negligible batch uptake of the same contaminant, which reflects the distinct nature of continuous-flow operation rather than improved sorption performance. Dynamic breakthrough integrates transient retention along the bed without allowing bulk re-equilibration, so a weakly sorbing analyte can produce a non-zero q_o even when batch equilibrium shows no net uptake. The rapid breakthrough for As(V) (τ = 53.0 min, the shortest among the three metals) confirms that arsenate retention remains limited under column operation, and the fitted q_o should not be interpreted as evidence of process-relevant retention capacity.

Taken together, the Pb(II) column results support its practical applicability for scaling, the Cd(II) column results require extended-operation verification before scaling, and the As(V) column results reinforce the conclusion from batch experiments that alkaline modification is insufficient for arsenate removal.

4.4. Kinetic and equilibrium modeling: Caveats

The non-linear regression analysis of kinetic data (Section 3.3; Table S7) requires careful interpretation. The pseudo-first-order (PFO) model provided the best overall fit for all three metals based on combined R^2, R^2adj, RMSE, χ^2, AICc, and qe,calc/qe,exp. agreement. This finding differs from the traditional interpretation in which PSO is associated with chemisorption and PFO with physisorption [34,49], but mechanistic assignment based solely on kinetic-model selection has been increasingly questioned [35,50,51]. The superior PFO fit for Cd(II) and Pb(II) is consistent with this critique: kinetic-model identity alone cannot determine mechanism, especially when complementary evidence (FTIR changes, pH dependence, pH_{PZC} shift, SEM observations) points to cation binding through ion exchange and surface complexation with oxygen-containing functional groups.

The comparison between PFO and PSO also supports reliance on multiple goodness-of-fit criteria rather than R^2 alone. PFO predicted qe values within 4–13% of experimental values, whereas PSO overestimated qe by 27% for As(V), 42% for Cd(II), and 57% for Pb(II) (Table S7) — a pattern consistent with published critiques of over-interpretation based on empirical kinetic-model identity [35,51]. For Cd(II) specifically, PFO and PSO were statistically indistinguishable by AICc (ΔAICc = 1.45; Table S7), meaning that model selection based on information criteria alone would not favor one over the other; the retention of PFO was therefore justified by the substantially better qe,

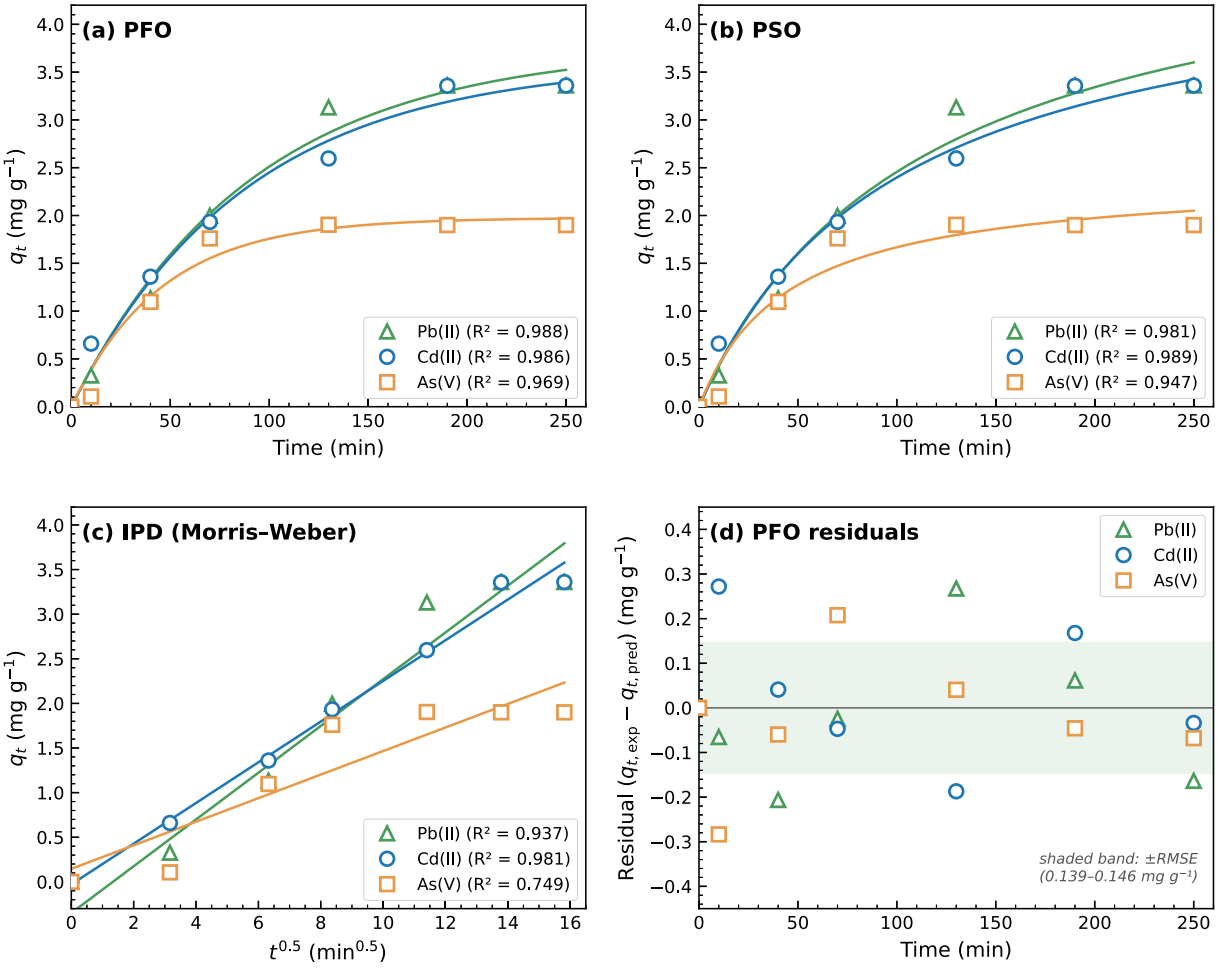


Fig. 3. Non-linear fitting of kinetic models to the apparent uptake of Pb(II), Cd(II), and As(V) by NaOH-modified olive stone: (a) pseudo-first-order (PFO), (b) pseudo-second-order (PSO), (c) intraparticle diffusion model (IPD; Weber–Morris), and (d) residuals of the PFO fits calculated as $q_{t,exp} - q_{t,pred}$. Symbols represent experimental data and solid lines represent non-linear model fits. The shaded band in (d) indicates the ±RMSE range (0.139–0.146 mg g^{-1}). Conditions: C_o = 50 mg L^{-1}, dosage = 15 g L^{-1}, 20 ± 2 °C, 200 rpm, with contaminant-specific optimal pH and particle size [Pb(II): pH 8.5, 150 μm; Cd(II): pH 6.0, 75 μm; As(V): pH 4.0, 150 μm].

calc/qe,exp. agreement (deviation 7.2% for PFO vs. 42% for PSO) [52]. The intraparticle diffusion model yielded a positive intercept for As(V) ($C = 0.146$) but negative intercepts for Cd(II) ($C = -0.028$) and Pb(II) ($C = -0.349$), the latter two lacking physical meaning as boundary-layer-related terms. The multilinearity observed in the qt versus $t^{0.5}$ plots (Fig. 3c) further indicates that a single-segment IPD model is inadequate for these data. Taken together, Pb(II) and Cd(II) uptake is more consistently explained by ion exchange and surface complexation than by kinetic-model identity alone, and no single kinetic or equilibrium model supports a definitive mechanistic conclusion for As(V).

The equilibrium experiments conducted at a single initial concentration ($C_o = 50$ mg L^{-1}) across three biosorbent dosages (Section 3.3; Table 3) produced narrow equilibrium concentration ranges unsuitable for reliable isotherm regression. Apparent uptake values are reported, but no maximum adsorption capacity (qmax) from Langmuir or Freundlich fitting is estimated, in contrast to many prior studies on olive-derived biosorbents [29,46,53,54]. This limitation is acknowledged explicitly and motivates the recommendation of multi-concentration equilibrium designs in future work (Section 4.8).

4.5. Operational viability and scalability

NaOH treatment was selected here as the most widely reported low-complexity alkaline activation route for lignocellulosic biosorbents [16,17] and has been applied to olive stone for heavy-metal removal [55]. Industrial-grade NaOH at ≈ USD 0.40 kg^{-1} is compatible with the very low cost of the olive-stone residue (≈ USD 0.05–0.10 kg^{-1} in Peruvian olive-producing regions; [21]), and the proposed treatment line is technically simple — milling, sieving, 0.1 M NaOH contact at room temperature for 24 h, washing to neutrality, drying at 60 °C — and compatible with existing post-harvest infrastructure in olive-producing regions. Three alternative routes deserve future evaluation as complementary or replacement strategies. Acid modification (H_3PO_4, citric acid) increases carboxylate density and surface area, but generally lowers pH_{PZC} and may further disfavor anion uptake [56]. Oxidative modification ($KMnO_4$, H_2O_2, ozone) introduces additional carboxyl and quinone groups, may improve Cd(II) uptake reproducibility, but adds reagent cost and operational complexity [56]. Metal-loaded modification (Fe(III), La(III), Al(III) impregnation following alkaline pretreatment) is the most promising route to address the As(V) limitation identified here, with reported Langmuir q_{max} of 74.8 mg g^{-1} for La(III)-watermelon rind [15] and 15.2 mg g^{-1} for Fe-impregnated henequen biochar [48]. A formal techno-economic analysis was beyond the scope of this study and is identified as a priority for the next stage (Section 4.8).

Regeneration: literature context and operational precedent. The present study does not report sorption–desorption cycling, and a dedicated regeneration campaign is identified as the next experimental phase (Section 4.8). We therefore make no quantitative claim regarding the regeneration efficiency of the present material. Two lines of indirect evidence are nonetheless relevant. First, olive-derived lignocellulosic materials have a well-documented regeneration profile in the literature: Blázquez et al. [29] reported 75–85% sustained Pb(II) capacity in NaOH-treated olive stone after three sorption–desorption cycles with HCl 0.1 M, and Calero et al. [26] reported 80–90% sustained capacity in olive pomace after five EDTA cycles. The NaOH-treated material reported here shares the cellulose–hemicellulose–lignin matrix of these reference materials, and the elevated mesoporosity (pore diameter 1.88 → 7.98 nm; Table S6) is favorable for diffusion-controlled desorption. This literature is used only to bound the plausible range and to justify the eluent selection for the planned campaign (HCl 0.1 M, EDTA 0.05 M, NaCl 0.1 M; ≥ 5 cycles; ≥ 80% retention criterion for Pb(II) prior to scale-up), not to predict the performance of this specific material. Second, the fixed-bed experiments provide a partial proxy for mechanical stability under continuous flow: the biosorbent retained its physical integrity over 250 min at 4 mL min^{-1} without channel formation, pressure-drop anomaly, or biosorbent fines in the effluent, and the breakthrough curves retained their expected sigmoidal shape (Fig. 4). This is not regeneration data, but it demonstrates the mechanical robustness that is a necessary precondition for any regeneration cycle.

4.6. Comparison with other biosorbents and treatment approaches

The performance of NaOH-modified olive stone can be contextualized against the broader literature on lignocellulosic biosorbents and alternative treatment approaches for the three contaminants (Table S8). For Pb(II), the experimental qe of 9.96 mg g^{-1} ($C_o = 50$ mg L^{-1}; 5 g L^{-1} dosage) is higher than values reported for untreated olive stone — 3.21 mg g^{-1} [46] and 6.57 mg g^{-1} [53] — but substantially lower than the 15.22 mg g^{-1} reported for olive stone modified with 2 M NaOH at $C_o =$ 150 mg L^{-1} [29]. This difference is consistent with both the more aggressive alkaline treatment (2 M vs. 0.1 M NaOH used here) and the higher initial concentration (150 vs. 50 mg L^{-1}), factors that cannot be fully disentangled with the available datasets. The implication for process design is that the intensity of alkaline treatment is an optimization variable with direct impact on sorption capacity, with associated trade-offs in terms of chemical consumption, washing requirements, and potential structural degradation of the biosorbent.

For Cd(II), q_e,exp. = 3.36 mg g^{-1} (kinetic series) and $q_o = 4.01$ mg g^{-1} (column) are comparable to, but slightly below, maximum capacities of untreated olive stone reported in prior studies (qmax = 3.56 mg g^{-1}, [46]; $q_{max} = 4.90$ mg g^{-1}, [53]). These comparisons, however, are based on qe values at single initial concentrations in the present study versus qmax values from multi-concentration Langmuir or Sips fits in the reference studies, and should not be interpreted as strict equivalences.

For As(V), the qe reported here is not comparable to the substantially higher values obtained with metal-loaded biosorbents designed for anion removal. La(III)-loaded watermelon rind achieved Langmuir q_{max} = 74.8 mg g^{-1} for As(V) [15], and Fe-impregnated henequen biochar reached $q_{max} = 15.2$ mg g^{-1} [48]. A broader pattern thus emerges from the literature: biosorbents modified with alkaline agents typically enhance cation removal but show poor affinity for anionic contaminants, whereas metal-loaded biosorbents achieve effective arsenate removal through positively charged surface sites. This contrast reflects a fundamental electrostatic constraint on lignocellulosic biosorbents: alkaline modification increases the density of negatively charged surface groups, favoring cation binding while reducing anion affinity at near-neutral and alkaline pH [7]. For process design, this pattern reinforces the contaminant-specific selection framework established in Section 4.2: a single surface modification cannot simultaneously optimize cation and anion retention, and treatment configurations should match surface chemistry to the dominant contaminant type.

4.7. Reproducibility and data availability

To support independent verification and re-analysis, the complete dataset and analysis scripts underlying this study are openly deposited at Zenodo (DOI: https://doi.org/10.5281/zenodo.19646178) under a Creative Commons Attribution 4.0 International (CC BY 4.0) license. The deposit includes the factorial batch data (pH × particle-size and dose × particle-size; raw ICP-OES outputs), the single-metal kinetic data (seven time points per metal), the fixed-bed breakthrough data, the physicochemical characterization outputs (chemical composition, FTIR, pH_{PZC} drift curves), and parallel R and Python scripts that reproduce the ANOVA, the partial eta-squared and partial omega-squared effect sizes, the noncentrality-inversion confidence intervals [39], and the non-linear kinetic and breakthrough-curve regressions. The reproducibility envelope is therefore extended beyond the manuscript itself: any reader can replicate the statistical inference and the model fits from the raw measurements, and any researcher can re-use the dataset for meta-analyses or alternative analytical approaches without further data requests.

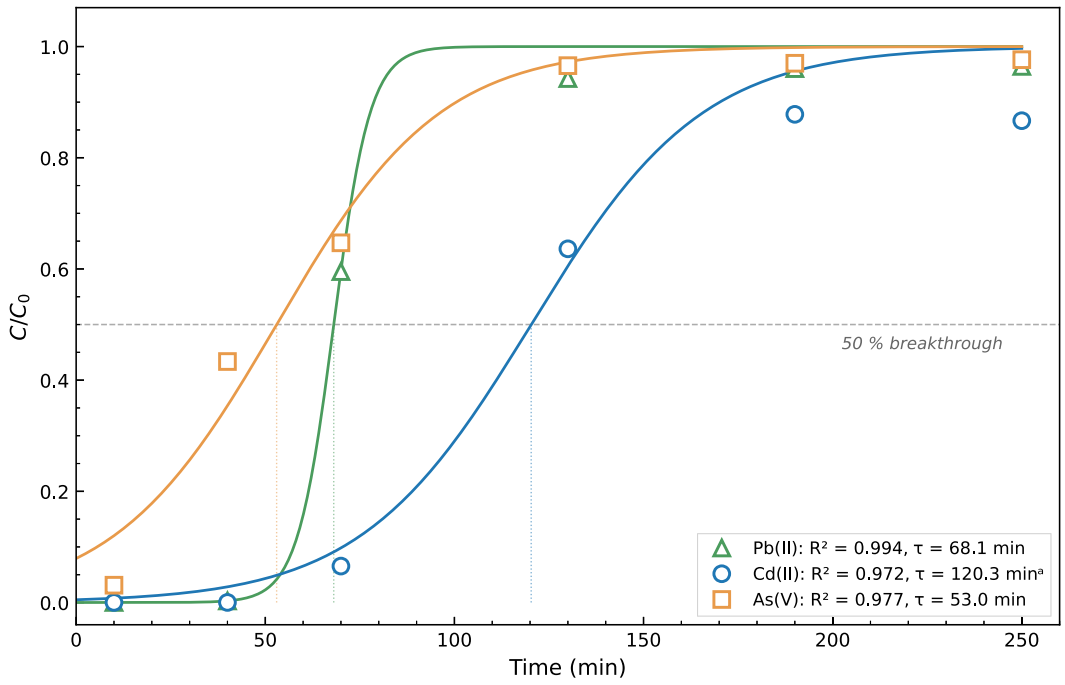


Fig. 4. Fixed-bed breakthrough curves for Pb(II), Cd(II), and As(V) removal by NaOH-modified olive stone. Symbols represent experimental data and solid lines represent non-linear Thomas model fits. Vertical dotted lines mark the 50% breakthrough time (τ) for each contaminant, with values reported in the legend together with the coefficient of determination (R^2). Conditions: C_0 = 50 mg L^{-1}, Q = 4 mL min^{-1}, m = 6 g, bed height = 9.5–10 cm, particle size = 300 μm. The dashed horizontal line indicates 50% breakthrough. [a] The Cd(II) curve did not reach complete saturation within the experimental runtime ($C/C_0 \approx 0.87$ at 250 min); the fitted Thomas parameters for Cd(II) therefore represent model-based extrapolations beyond the observed data range (see Table 4).

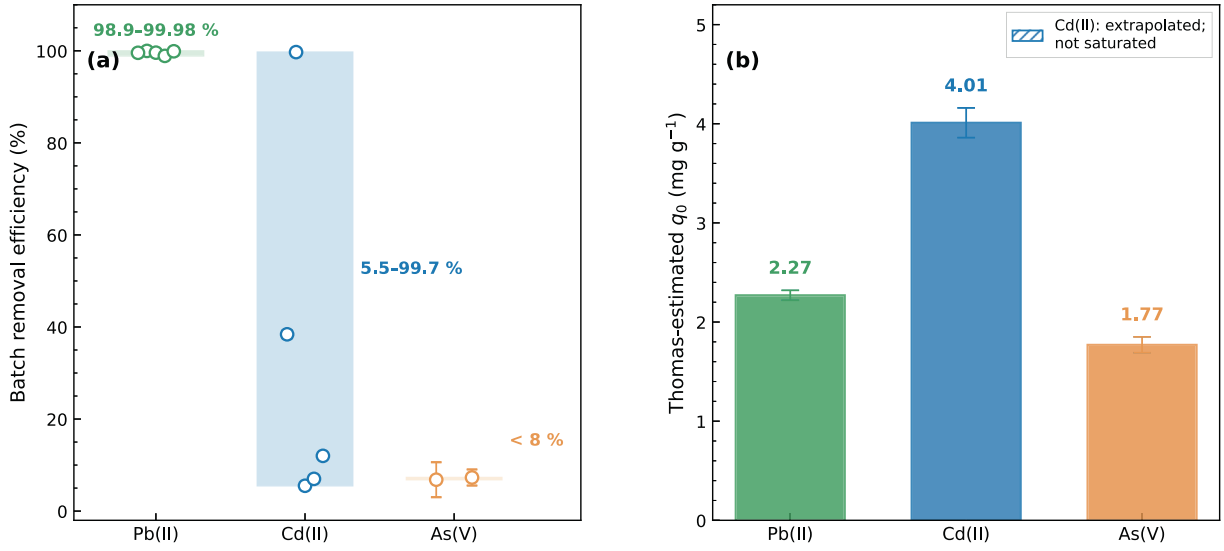


Fig. 5. Charge-dependent performance of NaOH-modified olive stone in batch and fixed-bed operation. (a) Inter-series batch removal efficiency for Pb(II), Cd(II), and As(V). Shaded bands indicate the observed inter-series minimum–maximum range; open symbols represent individual experimental series (two factorial-design optima and three equilibrium dose series). Error bars are within-series standard deviations where available. The As(V) equilibrium series showed Ce > C_0 (n.d.; Table 3) and is not included in the band. (b) Thomas model-estimated column capacity (q_0); operating conditions: C_0 = 50 mg L^{-1}, Q = 4 mL min^{-1}, m = 6 g, particle size = 300 μm. Error bars represent regression uncertainty. The Cd(II) bar is hatched because the breakthrough curve did not reach complete saturation within the 250-min window; q_0 for Cd(II) is therefore a model-based extrapolation.

4.8. Limitations and future perspectives

Three study-specific limitations require particular emphasis as direct consequences of the design choices in this study. **First**, the pH × particle-size factorial employed different buffer systems across pH levels (citrate at pH 4.0 and 6.0; phosphate at pH 6.8 and 8.0; borate at pH 8.5). Because phosphate competes with arsenate for oxyanion sorption sites and precipitates Pb(II) as $Pb_3(PO_4)_2$, and because citrate chelates Pb(II) and Cd(II) (log K ≈ 4.1 and 3.8 respectively; [33]), the interpretation of pH as an independent factor is partially confounded with buffer identity at pH 4.0, 6.0, 6.8, and 8.0. The factorial optimum identified for Pb(II) (pH 8.5, borate) is not affected by this confound, but Pb(II) removal reported at pH 6.8 and 8.0 should be interpreted as upper-bound apparent removal. Future studies should employ non-complexing, non-

competing buffers (MES, HEPES) or manual pH titration to disentangle pH and buffer effects. **Second**, equilibrium experiments were performed at a single initial concentration ($C_o = 50$ mg L^{-1}) across three biosorbent dosages, which produces narrow equilibrium concentration ranges unsuitable for reliable Langmuir or Freundlich regression; no maximum adsorption capacity is reported in this study, and multi-concentration isotherm campaigns (10–200 mg L^{-1} at fixed dose) are required for direct comparison with literature qmax values. **Third**, regeneration, desorption, and reusability over multiple cycles were not assessed; this limits the immediate translational value of the present results and is identified as a defined next step. **Fourth**, the inter-series discrepancy in Cd(II) removal (99.7% vs. 38.4% vs. 5.5–12.0%; Sections 3.3 and 4.1) is attributable to operational differences between series (dose, contact time, replication regime) quantified in the supplementary Table S9; potential biosorbent batch variability could not be evaluated because a single NaOH-modification preparation was used (Section 2.2), and multi-batch characterization remains a recommended next step. **Fifth**, the present study evaluates As(V) and does not address As(III); evaluation under reducing conditions, likely requiring an oxidative pretreatment or an iron-modified material, is required for a complete arsenic-treatment assessment. **Sixth**, two replicates per factorial cell limited residual degrees of freedom and inflated η^2p estimates for Pb(II); triplicate replication should become standard in future studies of this type. **Seventh**, the chemical and lignocellulosic characterization (Table S4) was performed as single determinations on three fractions from a single biosorbent preparation, which does not permit inferential NC–CT comparison; analytical replication ($n \geq 3$ per fraction) is recommended.

Several additional methodological considerations apply. All experiments used synthetic single-metal solutions; competitive adsorption in multi-metal systems may substantially alter removal efficiencies and selectivity. The tested pH range (4.0–8.5) excluded strongly acidic and strongly alkaline conditions under which As(V) and Pb(II) speciation would differ. The fixed-bed column used a single coarse particle size (300 μm, selected to minimize pressure drop), partially constraining batch–column comparison (Section 4.3). The kinetic experiments used seven sampling times over 250 min; additional early-time points (within the first 30 min) would improve rate-constant precision and model discrimination. The $Ce > C_o$ pattern observed for As(V) (Section 4.1) could not be unambiguously attributed to contaminant mobilization without dedicated blank leaching controls (CT in metal-free buffered solution), which should become routine in future studies of modified lignocellulosic biosorbents.

Future research should therefore prioritize: (i) multi-concentration isotherm characterization (10–200 mg L^{-1} at fixed dose) for Pb(II) and Cd(II) under non-complexing buffers (MES, HEPES) to disentangle equilibrium parameters from the buffer-related confounds identified here; (ii) multi-cycle adsorption–desorption testing (HCl 0.1 M, EDTA 0.05 M, NaCl 0.1 M as candidate eluents) over at least five cycles, with the criterion of ≥80% regeneration efficiency for Pb(II) before scale-up; (iii) development of Fe(III)-modified olive stone to test the dual-modification strategy proposed in Section 4.5, and evaluation under reducing conditions and against As(III); (iv) competitive adsorption in multi-metal synthetic systems and in real wastewaters representative of mining, electroplating, and agricultural runoff; (v) techno-economic and life-cycle analyses comparing NaOH-modified olive stone with conventional treatment technologies; and (vi) blank leaching and non-complexing buffer controls to cleanly disentangle buffer identity from pH effects, particularly for As(V).

5. Conclusions

This study evaluated NaOH-modified olive stone (*Olea europaea* L.) for the removal of cationic Pb(II) and Cd(II) and anionic As(V) in batch and fixed-bed column systems, testing whether alkaline surface modification produces a consistent pattern of charge-dependent performance within the same biosorbent and across both operational modes. Alkaline treatment shifted the pH_{PZC} from 4.47 to 6.83, increased the average pore diameter from 1.88 to 7.98 nm, and produced compositional and spectroscopic changes consistent with ester-bond saponification and greater exposure of carboxylate- and hydroxyl-containing surface groups. These modifications translated into clearly differentiated performance outcomes for the three contaminants.

Under optimized batch conditions, Pb(II) removal reached 99.57% and remained consistently high across all experimental series (>98.9%), with pH as the dominant factor ($\eta^2p = 0.997$). Removal at pH 6.8 and 8.0 should be interpreted as upper bounds because the phosphate buffer used at those pH levels can contribute through lead phosphate precipitation; the factorial optimum (pH 8.5, borate buffer) is not affected by this confound. Cd(II) removal varied from 5.5% to 99.72% depending on operational conditions, with the upper value obtained in the dose × particle-size factorial at 15 g L^{-1} and the lower bound in the equilibrium series at 250 min. The variability is largely attributable to operational differences between experimental series — dose, contact time, and replication regime — quantified in Table S9; since a single biosorbent preparation was used throughout, batch-to-batch variability could not be evaluated and remains a recommended next step. As(V) removal remained below 8% under all tested conditions, with the $C_e > C_o$ pattern observed in the equilibrium series interpreted cautiously as evidence of poor and unstable arsenate retention rather than as demonstrated contaminant release. Fixed-bed column performance was adequately described by Thomas and Yoon–Nelson models ($R^2 > 0.97$), with column capacities following Cd(II) (4.01 mg g^{-1}) > Pb(II) (2.27 mg g^{-1}) > As(V) (1.77 mg g^{-1}); this ranking reflects different operational conditions between batch and column experiments rather than a reversal of intrinsic affinity.

The practical implications for water treatment process design are threefold. First, NaOH-modified olive stone is a viable, reproducible option for Pb(II) removal from cation-dominated effluents (e.g., electroplating, battery manufacturing, mining), with treatment targets achievable at dosages within the tested range (5–15 g L^{-1}). Second, the material is usable for Cd(II) but requires standardized operational protocols (dosage and contact time), pre-implementation testing on the specific effluent, and dose control above the operational threshold (≥ 15 g L^{-1}) to ensure consistent performance; the >99% Cd(II) removal observed under optimized conditions should therefore be interpreted as upper-bound performance rather than as a uniformly reproducible property. Third, the material is unsuitable for arsenate-containing waters, and effective anion removal would require alternative surface modifications (e.g., Fe(III)- or La(III)-loaded biosorbents) that generate positively charged sorption sites. For mixed cation–anion effluents, the charge-dependent performance documented here implies that a single alkaline-modified material is insufficient: sequential treatment configurations or bifunctional materials combining cation- and anion-binding domains are more promising design directions.

Taken together, these results demonstrate that NaOH modification does not produce a general-purpose biosorbent but rather a contaminant-specific treatment option, and support a selection framework based on the charge of the target contaminant. This perspective reframes biosorbent evaluation from “does it remove contaminant X?” to “for which contaminant type is this surface chemistry appropriate?” — a question that places process-design considerations at the center of biosorbent assessment.

Three priorities should guide the next stage of this research line. First, a multi-concentration isotherm campaign (10–200 mg L^{-1} at fixed dose) for Pb(II) and Cd(II) under non-complexing buffers (MES, HEPES) to disentangle equilibrium parameters from the buffer-related confounds identified here. Second, multi-cycle adsorption–desorption testing (HCl 0.1 M, EDTA 0.05 M, NaCl 0.1 M as candidate eluents) over at least five cycles, with the criterion of ≥80% regeneration efficiency for Pb(II) before scale-up. Third, evaluation under reducing conditions and against As(III), most likely through Fe(III) or La(III) impregnation of

the NaOH-treated material, to address the anionic-contaminant limitation identified for the present formulation. Until these milestones are completed, NaOH-modified olive stone should be considered viable specifically for Pb(II) removal from cation-dominated effluents free of competing phosphate, conditionally applicable for Cd(II) subject to standardized operating conditions (dosage and contact time), and unsuitable for As(V) or any arsenate-bearing matrix.

CRediT authorship contribution statement

Jose A. Valeriano-Zapana: Writing – review & editing, Supervision, Project administration, Methodology, Investigation, Funding acquisition, Formal analysis, Conceptualization. **Vera D. Condori-Yupanqui:** Validation, Investigation, Data curation. **Paulino F. Rios-Zapana:** Validation, Supervision, Investigation. **Juana J. Melendez-Mier:** Resources, Investigation. **Leonel A. Paccosonco-Sucapuca:** Investigation, Formal analysis. **Corina A. Vera-Gonzáles:** Writing – review & editing, Supervision, Resources, Methodology. **Juan A. Lopa-Bolívar:** Writing – review & editing, Supervision.

Funding

This research was supported by the National Program of Scientific Research and Advanced Studies (PROCIENCIA) of the National Council of Science, Technology, and Technological Innovation (CONCYTEC), Peru, under Contract No. 365–2019-FONDECYT, awarded to J.A. Valeriano-Zapana. The funding source had no involvement in study design, data collection, analysis, interpretation, writing of the report, or decision to submit the article for publication.

Declaration of competing interest

The authors declare that they have no known competing financial interests or personal relationships that could have appeared to influence the work reported in this paper.

Acknowledgments

The authors gratefully acknowledge the olive producers of the Algarrobal Valley (Ilo, Moquegua, Peru) for their field support and provision of raw olive stone material. Biosorbent characterization (SEM, BET, FTIR) was performed at the Facultad de Ciencias, Universidad Nacional de Ingeniería (UNI, Lima, Peru). Metal quantification by ICP-OES was conducted by CERPER S.A. (Arequipa, Peru).

Appendix A. Supplementary data

Supplementary data to this article can be found online at https://doi.org/10.1016/j.jwpe.2026.110500.

Data availability

The raw experimental data and analysis scripts supporting this study are openly available in the Zenodo repository under a Creative Commons Attribution 4.0 International (CC BY 4.0) license (DOI: https://doi.org/10.5281/zenodo.19646178; [58]). The deposit includes factorial batch data, single-metal kinetic data, fixed-bed column breakthrough data, physicochemical characterization data (ash, Fe, P, Ca + Mg, FTIR, pHPZC), the full ANOVA output (sums of squares, mean squares, F statistics), and parallel R and Python scripts used for the statistical and nonlinear regression analyses reported in the manuscript.

References

[1] M. Balali-Mood, K. Naseri, Z. Tahergorabi, M.R. Khazdair, M. Sadeghi, Toxic mechanisms of five heavy metals: mercury, lead, chromium, cadmium, and arsenic, Front. Pharmacol. (2021), https://doi.org/10.3389/fphar.2021.643972.
[2] B.A. Sadee, S.M.S. Zebari, Y. Galali, M.F. Saleem, A review on arsenic contamination in drinking water: sources, health impacts, and remediation approaches, RSC Adv. (2025), https://doi.org/10.1039/d4ra08867k.
[3] B.R. Shetty, P.B. Jagadeesha, S.A. Salmataj, Heavy metal contamination and its impact on the food chain: exposure, bioaccumulation, and risk assessment, CYTA J. Food (2025), https://doi.org/10.1080/19476337.2024.2438726.
[4] P. Sevak, B. Pushkar, Arsenic pollution cycle, toxicity and sustainable remediation technologies: a comprehensive review and bibliometric analysis, J. Environ. Manag. 349 (2024) 119504, https://doi.org/10.1016/J.JENVMAN.2023.119504.
[5] J. Bundschuh, N.K. Niazi, M.A. Alam, M. Berg, I. Herath, B. Tomaszewska, J. P. Maity, Y.S. Ok, Global arsenic dilemma and sustainability, J. Hazard. Mater. 436 (2022), https://doi.org/10.1016/j.jhazmat.2022.129197.
[6] M.A. Carneiro, A.M.A. Pintor, R.A.R. Boaventura, C.M.S. Botelho, Current trends of arsenic adsorption in continuous mode: literature review and future perspectives, Sustainability (2021), https://doi.org/10.3390/su13031186.
[7] L.C. Maia, L.C. Soares, L.V. Alves Gurgel, A review on the use of lignocellulosic materials for arsenic adsorption, J. Environ. Manag. 288 (2021) 112397, https://doi.org/10.1016/j.jenvman.2021.112397.
[8] S. Ambika, M. Kumar, L. Pisharody, M. Malhotra, G. Kumar, V. Sreedharan, L. Singh, P.V. Nidheesh, A. Bhatnagar, Modified biochar as a green adsorbent for removal of hexavalent chromium from various environmental matrices: mechanisms, methods, and prospects, Chem. Eng. J. (2022), https://doi.org/10.1016/j.cej.2022.135716.
[9] P.R. Yaashikaa, J. Palanivelu, R.V. Hemavathy, Sustainable approaches for removing toxic heavy metal from contaminated water: a comprehensive review of bioremediation and biosorption techniques, Chemosphere 357 (2024) 141933, https://doi.org/10.1016/J.CHEMOSPHERE.2024.141933.
[10] S. Meftah, K. Meftah, N. Babassa, K. Malous, M. Drissi, A. Amahrous, N. Jabri, J. Fathi, K. Aguerchi, Y. Laababid, O. Adnouss, M. Taib, O. Zinaoui, O. ElHassan, L. Bouyazza, The versatility and effectiveness of bio-adsorbents in the removal of chemical pollutants from water: adsorption mechanisms, optimization by ANN and RSM, SWOT analysis, and contribution to the 3rd and 6th Sustainable Development Goals, Discov. Sustain. (2025), https://doi.org/10.1007/s43621-025-01359-7.
[11] Staszak, K., Regel-Rosocka, M., 2024. Removing heavy metals: cutting-edge strategies and advancements in biosorption technology. Materials 2024, Vol. 17, Page 1155 17, 1155. doi:https://doi.org/10.3390/MA17051155.
[12] A.A. Beni, A. Esmaeili, Biosorption, an efficient method for removing heavy metals from industrial effluents: a review, Environ. Technol. Innov. (2020), https://doi.org/10.1016/j.eti.2019.100503.
[13] M. Bilal, I. Ihsanullah, M. Younas, M. Ul Hassan Shah, Recent advances in applications of low-cost adsorbents for the removal of heavy metals from water: a critical review, Sep. Purif. Technol. (2022), https://doi.org/10.1016/j.seppur.2021.119510.
[14] H. Qin, T. Hu, Y. Zhai, N. Lu, J. Aliyeva, The improved methods of heavy metals removal by biosorbents: a review, Environ. Pollut. 258 (2020) 113777, https://doi.org/10.1016/j.envpol.2019.113777.
[15] R.L. Aryal, A. Thapa, B.R. Poudel, M.R. Pokhrel, B. Dahal, H. Paudyal, K. N. Ghimire, Effective biosorption of arsenic from water using La(III) loaded carboxyl functionalized watermelon rind, Arab. J. Chem. 15 (2022) 103674, https://doi.org/10.1016/j.arabjc.2021.103674.
[16] H.I. Syeda, I. Sultan, K.S. Razavi, P.S. Yap, Biosorption of heavy metals from aqueous solution by various chemically modified agricultural wastes: a review, J. Water Process Eng. 46 (2022) 102446, https://doi.org/10.1016/J.JWPE.2021.102446.
[17] H.N. Tran, Adsorption technology for water and wastewater treatments, Water (2023), https://doi.org/10.3390/w15152857.
[18] Bouharat, D., Bouzit, L., Nechar, M., Laghdach, A. EL, Yousfi, F. EL, 2024. Kinetics, isotherm, and thermodynamic parameters of polyphenol adsorption from olive mill wastewater onto activated carbon. J. Mater. Environ. Sci. 2024, 1736–1747.
[19] A. Karnwal, Unveiling the promise of biosorption for heavy metal removal from water sources, Desalin. Water Treat. (2024), https://doi.org/10.1016/j.dwt.2024.100523.
[20] G. Enaime, S. Dababat, M. Wichern, M. Lübken, Olive mill wastes: from wastes to resources, Environ. Sci. Pollut. Res. (2024), https://doi.org/10.1007/s11356-024-32468-x.
[21] MIDAGRI, Guía Técnica del Cultivo de Olivo en la Región Tacna, Ministerio de Desarrollo Agrario y Riego, Lima, Peru, 2022.
[22] J.F. Lustosa Filho, A.P.F. da Silva, S.T. Costa, H.T. Gomes, T. de Figueiredo, Z. Hernández, Biochars derived from olive mill byproducts: typology, characterization, and eco-efficient application in agriculture—a systematic review, Sustainability (2024), https://doi.org/10.3390/su16125004.
[23] M. Rodríguez-Pérez, B. García-Béjar, E. Burgos-Ramos, P. Silva, Valorization of Olive Oil and Wine Industry Byproducts: Challenges and Opportunities in Sustainable Food Applications, Foods (2025), https://doi.org/10.3390/foods14142475.
[24] Y. Bakhtaoui, M. Ben Ali, M. Ouakki, O. El Khattabi, N. El Azzouzi, B. Srhir, Efficient adsorption of methylene blue onto raw olive pomace from Moroccan industrial oil mills: linear and nonlinear isotherm and kinetic modeling with error analysis, Next Materials 9 (2025), https://doi.org/10.1016/j.nxmate.2025.101072.

[25] D.O. Ozcan, Hendekcï, M. C., B. Ovez, Enhancing the adsorption capacity of organic and inorganic pollutants onto impregnated olive stone derived activated carbon, Heliyon 10 (2024), https://doi.org/10.1016/j.heliyon.2024.e32792.
[26] M. Calero, I. Iáñez-Rodríguez, A. Pérez, M.A. Martín-Lara, G. Blázquez, Neural fuzzy modelization of copper removal from water by biosorption in fixed-bed columns using olive stone and pinion shell, Bioresour. Technol. 252 (2018) 100–109, https://doi.org/10.1016/j.biortech.2017.12.074.
[27] M.A. Martín-Lara, I.L. Rodríguez, G. Blázquez, M. Calero, Factorial experimental design for optimizating the removal conditions of lead ions from aqueous solutions by three wastes of the olive-oil production, Desalination 278 (2011) 132–140, https://doi.org/10.1016/j.desal.2011.05.016.
[28] A. Abdolali, H.H. Ngo, W. Guo, J.L. Zhou, B. Du, Q. Wei, X.C. Wang, P.D. Nguyen, Characterization of a multi-metal binding biosorbent: chemical modification and desorption studies, Bioresour. Technol. 193 (2015) 477–487, https://doi.org/10.1016/j.biortech.2015.06.123.
[29] G. Blázquez, M. Calero, A. Ronda, G. Tenorio, M.A. Martín-Lara, Study of kinetics in the biosorption of lead onto native and chemically treated olive stone, J. Ind. Eng. Chem. 20 (2014) 2754–2760, https://doi.org/10.1016/J.JIEC.2013.11.003.
[30] P.J. Van Soest, J.B. Robertson, B.A. Lewis, Methods for dietary fiber, neutral detergent fiber, and nonstarch polysaccharides in relation to animal nutrition, J. Dairy Sci. 74 (1991) 3583–3597, https://doi.org/10.3168/JDS.S0022-0302(91)78551–2.
[31] E.N. Bakatula, D. Richard, C.M. Neculita, G.J. Zagury, Determination of point of zero charge of natural organic materials, Environ. Sci. Pollut. Res. 25 (2018) 7823–7833, https://doi.org/10.1007/s11356-017-1115-7.
[32] Smičiklas, I.D., Milonjić, S.K., Pfendt, P., Raičević, S., 2000. The point of zero charge and sorption of cadmium (II) and strontium (II) ions on synthetic hydroxyapatite. Sep. Purif. Technol. 18, 185–194. doi:https://doi.org/10.1016/S1383-5866(99)00066-0.
[33] R.M. Smith, A.E. Martell, R.J. Motekaitis, NIST Standard Reference Database 46: NIST Critically Selected Stability Constants of Metal Complexes, Version 8.0, National Institute of Standards and Technology, Gaithersburg, MD, 2004.
[34] Ho, Y.S., McKay, G., 1999. Pseudo-second order model for sorption processes. Process Biochem. 34, 451–465. doi:https://doi.org/10.1016/S0032-9592(98)00112-5.
[35] J.P. Vareda, On validity, physical meaning, mechanism insights and regression of adsorption kinetic models, J. Mol. Liq. 376 (2023) 121416, https://doi.org/10.1016/J.MOLLIQ.2023.121416.
[36] H.C. Thomas, Heterogeneous ion exchange in a flowing system, J. Am. Chem. Soc. 66 (1944) 1664–1666, https://doi.org/10.1021/JA01238A017.
[37] P. Virtanen, R. Gommers, T.E. Oliphant, M. Haberland, T. Reddy, D. Cournapeau, et al., SciPy 1.0: fundamental algorithms for scientific computing in Python, Nat. Methods 17 (2020) 261–272, https://doi.org/10.1038/s41592-019-0686-2.
[38] Y.H. Yoon, J.H. Nelson, Application of gas adsorption kinetics I. A theoretical model for respirator cartridge service life, Am. Ind. Hyg. Assoc. J. 45 (1984) 509–516, https://doi.org/10.1080/15298668491400197.
[39] J.H. Steiger, Beyond the F test: effect size confidence intervals and tests of close fit in the analysis of variance and contrast analysis, Psychol. Methods 9 (2004) 164–182, https://doi.org/10.1037/1082-989X.9.2.164.
[40] S. Olejnik, J. Algina, Generalized eta and omega squared statistics: measures of effect size for some common research designs, Psychol. Methods 8 (2003) 434–447, https://doi.org/10.1037/1082-989X.8.4.434.
[41] J.T.E. Richardson, Eta squared and partial eta squared as measures of effect size in educational research, Educ. Res. Rev. 6 (2011) 135–147, https://doi.org/10.1016/j.edurev.2010.12.001.
[42] R Core Team, R: A Language and Environment for Statistical Computing, R Foundation for Statistical Computing, Vienna, 2025. Austria, https://www.R-project.org/.
[43] D.J. Stanley, J.R. Spence, Reproducible tables in psychology using the apaTables package, Adv. Methods Pract. Psychol. Sci. 1 (2018) 415–431, https://doi.org/10.1177/2515245918773743.
[44] H.N. Rabetafika, B. Bchir, C. Blecker, M. Paquot, B. Wathelet, Comparative study of alkaline extraction process of hemicelluloses from pear pomace, Biomass Bioenergy 61 (2014) 254–264, https://doi.org/10.1016/j.biombioe.2013.12.022.
[45] H. Paudyal, S. Adhikari, K. Nath Ghimire, D. Gyawali, I. Raj Upadhyaya, B. Dahal, M. Raj Pokhrel, Synthesis, characterization and cation exchange performance of chemically modified pineapple waste biomass for the removal of Fe(II) from water, Results Chem. 4 (2022), https://doi.org/10.1016/j.rechem.2022.100608.
[46] N. Fiol, I. Villaescusa, M. Martínez, N. Miralles, J. Poch, J. Serarols, Sorption of Pb (II), Ni(II), Cu(II) and Cd(II) from aqueous solution by olive stone waste, Sep. Purif. Technol. 50 (2006) 132–140, https://doi.org/10.1016/j.seppur.2005.11.016.
[47] F. Pagnanelli, S. Mainelli, F. Vegliò, L. Toro, Heavy metal removal by olive pomace: biosorbent characterisation and equilibrium modelling, Chem. Eng. Sci. 58 (2003) 4709–4717, https://doi.org/10.1016/j.ces.2003.08.001.
[48] Liao, X., Miranda Avilés, R., Serafin Muñoz, A.H., Rocha Amador, D.O., Perez Rodriguez, R.Y., Hernández Anguiano, J.H., Julia Navarro, C., Zha, X., Moncada, D., de Jesús Puy Alquiza, M., Vinod Kshirsagar, P., Li, Y., 2024. Efficient arsenic removal from water using iron-impregnated low-temperature biochar derived from henequen fibers: performance, mechanism, and LCA analysis. Sci. Rep. 2024 14:1 14, 20769-. doi:https://doi.org/10.1038/s41598-024-69769-7.
[49] D. Park, Y.S. Yun, J.M. Park, The past, present, and future trends of biosorption, Biotechnol. Bioprocess Eng. (2010), https://doi.org/10.1007/s12257-009-0199-4.
[50] Y. Liu, Y.J. Liu, Biosorption isotherms, kinetics and thermodynamics, Sep. Purif. Technol. 61 (2008) 229–242, https://doi.org/10.1016/j.seppur.2007.10.002.
[51] H.N. Tran, S.J. You, A. Hosseini-Bandegharaei, H.P. Chao, Mistakes and inconsistencies regarding adsorption of contaminants from aqueous solutions: a critical review, Water Res. 120 (2017) 88–116, https://doi.org/10.1016/J.WATRES.2017.04.014.
[52] K.P. Burnham, D.R. Anderson, Model Selection and Multimodel Inference: A Practical Information-Theoretic Approach, second ed, Springer, New York, 2002, https://doi.org/10.1007/b97636.
[53] F. Hernáinz, M. Calero, G. Blázquez, M.A. Martín-Lara, G. Tenorio, Comparative study of the biosorption of cadmium(II), chromium(III), and lead(II) by olive stone, Environ. Prog. 27 (2008) 469–478, https://doi.org/10.1002/ep.10299.
[54] A. Ronda, M.A. Martín-Lara, G. Blázquez, N. Moreno, M. Calero, Copper biosorption in the presence of lead onto olive stone and pine bark in batch and continuous systems, Environ. Prog. Sustain. Energ. 33 (2014) 192–204, https://doi.org/10.1002/ep.11780.
[55] M.A. Martín-Lara, G. Blázquez, A. Ronda, A. Pérez, M. Calero, Development and characterization of biosorbents to remove heavy metals from aqueous solutions by chemical treatment of olive stone, Ind. Eng. Chem. Res. 52 (2013) 10809–10819, https://doi.org/10.1021/ie401246c.
[56] M.A. Martín-Lara, F. Pagnanelli, S. Mainelli, M. Calero, L. Toro, Chemical treatment of olive pomace: effect on acid-basic properties and metal biosorption capacity, J. Hazard. Mater. 156 (2008) 448–457, https://doi.org/10.1016/j.jhazmat.2007.12.035.
[57] H. Zeng, Y. Yu, F. Wang, J. Zhang, D. Li, Arsenic(V) removal by granular adsorbents made from water treatment residuals materials and chitosan, Colloids Surf. A Physicochem. Eng. Asp. 585 (2020) 124036, https://doi.org/10.1016/J.COLSURFA.2019.124036.
[58] Valeriano-Zapana, J.A., Condori-Yupanqui, V.D., Rios-Zapana, P.F., Melendez-Mier, J.J., Paccosonco-Sucapuca, L.A., Vera-Gonzáles, C.A., Lopa Bolívar, J.A., 2026. Olive Stone Biosorption Dataset, Version 1.0 [Data set]. Zenodo. doi: https://doi.org/10.5281/zenodo.19646178.